ISSN 1063-7761, Journal of Experimental and Theoretical Physics, 2015, Vol. 120, No. 1, pp. 15–48. © Pleiades Publishing, Inc., 2015.
Original Russian Text © N.A. Inogamov, V.V. Zhakhovskii, V.A. Khokhlov, 2015, published in Zhurnal Eksperimental'noi i Teoreticheskoi Fiziki, 2015, Vol. 147, No. 1, pp. 20–56.

Jet Formation in Spallation of Metal Film from Substrate under Action of Femtosecond Laser Pulse

N. A. Inogamov[a], **V. V. Zhakhovskii**[b], **and V. A. Khokhlov**[a]

[a] *Landau Institute for Theoretical Physics, Russian Academy of Sciences, Chernogolovka, Moscow oblast, 142432 Russia*
[b] *Dukhov All-Russia Research Institute of Automatics, Rosatom, Moscow, 127055 Russia*
e-mail: nailinogamov@googlemail.com

Received August 20, 2014

Abstract—It is well known that during ablation by an ultrashort laser pulse, the main contribution to ablation of the substance is determined not by evaporation, but by the thermomechanical spallation of the substance. For identical metals and pulse parameters, the type of spallation is determined by film thickness d_f. An important gauge is metal heating depth d_T at the two-temperature stage, at which electron temperature is higher than ion temperature. We compare cases with $d_f < d_T$ (thin film) and $d_f \gg d_T$ (bulk target). Radius R_L of the spot of heating by an optical laser is the next (after d_f) important geometrical parameter. The morphology of film bulging in cases where $d_f < d_T$ on the substrate (blistering) changes upon a change in radius R_L in the range from diffraction limit $R_L \sim \lambda$ to high values of $R_L \gg \lambda$, where $\lambda \sim 1$ μm is the wavelength of optical laser radiation. When $d_f < d_T$, $R_L \sim \lambda$, and $F_{\rm abs} > F_{\rm m}$, gold film deposited on the glass target acquires a cupola-shaped blister with a miniature frozen nanojet in the form of a tip on the circular top of the cupola ($F_{\rm abs}$ and $F_{\rm m}$ are the absorbed energy and the melting threshold of the film per unit surface area of the film). A new physical mechanism leading to the formation of the nanojet is proposed.

DOI: 10.1134/S1063776115010136

1. INTRODUCTION

A large number of modern technologies are based on the application of ultrashort laser pulses (USLPs) of duration $\tau_L \sim 0.01$–1 ps. These technologies include the formation of hollow blisters on the film surface; the structuring of films for biological applications and microelectronics; the enhancement of the static electric field at the at the tips of miniature jets crowning hollow bumps; the transport of microscopic pieces of the film from the substrate to the receiver (laser printing); and so on. Detailed lists of corresponding references are given in recent publications [1, 2] devoted to the analysis of blistering and nanojets. Beginning with publications [3, 4], it has been known that mechanical effects and hydrodynamic flows induced by them play an important role in the case of USLPs. The thermomechanical effects are pronounced when the condition of ultrasonic heating is satisfied. Under this condition, the duration τ_T of the formation of a heated layer of thickness d_T is smaller than the sound time $t_s = d_T/c_s$ over which a hydrodynamic perturbation propagates through the heated layer with velocity of sound c_s. Accordingly, the phase velocity d_T/τ_T of the formation of the heated layer is higher than the velocity of sound.

When an optical USLP is acting on a thick metal target, scales τ_T and d_T are determined by the following two main factors. The first factor is the duration of two-temperature (2T) relaxation $t_{\rm eq}$ ($\tau_T = t_{\rm eq}$), at the end of which electron temperature T_e and ion temperature T_i become approximately equal. Second, it is electron thermal conductivity κ_{2T} in the 2T state (see, for example, [5] and the literature cited therein); usually, $t_{\rm eq} \approx 2$–7 ps, $d_T \approx 50$–140 nm, and $t_s \approx 10$–30 ps. The estimates based on the heat balance equations $C_i\partial T_i/\partial t = \alpha(T_e - T_i)$ for electrons and ions [6] have the form

$$t_{\rm eq} \approx \frac{C_i}{\alpha}\frac{(T_i)_{\rm fin}}{(T_e)_{\rm max}} \sim \frac{\sqrt{\gamma/2}}{\alpha}\frac{(E_i)_{\rm max}}{\sqrt{(E_e)_{\rm max}}}, \qquad (1)$$

$$d_T \approx \sqrt{\chi_{2T}t_{\rm eq}}, \quad \chi_{2T} = \frac{\kappa_{2T}}{C_e}, \qquad (2)$$

where C_i and $C_e = \gamma T_e$ are the ion and electron heat capacities, E_i and E_e are the internal energies of the ion and electron subsystems, $\gamma \sim 100$ J m^{-3} K^{-2}, $(T_i)_{\rm fin}$ is temperature of ions and electrons at the end of the 2T stage, $(T_e)_{\rm max}$ is the maximal electron temperature at the 2T stage, and $\alpha \sim 10^{17}$ W K^{-1} m^{-3} is the coefficient of the electron–ion exchange energy in the condensed medium [7–9].[1] The maximum of ion energy $(E_i)_{\rm max}$ is attained at the end of the 2T stage.

---

[1] The coefficient α for the dielectric was calculated in [10]. In [7–9], the values of α were calculated only for metals.

If we assume approximately that $(E_i)_{\max} \sim (E_e)_{\max}$ and substitute this estimate into relations (1) and (2), we obtain

$$t_{\rm eq} \sim \frac{(\gamma/2)^{2/5}}{\alpha^{4/5}\chi_{2T}^{1/5}} F_{\rm abs}^{2/5} \sim 8[\text{ps}]\frac{\gamma_{100}^{2/5}}{\alpha_{17}^{4/5}\chi_{10}^{1/5}} F_{100}^{2/5},$$

$$d_T \sim 90[\text{nm}]\frac{\gamma_{100}^{1/5}\chi_{10}^{2/5}}{\alpha_{17}^{2/5}} F_{100}^{1/5},$$

where $\gamma_{100} = \gamma/100$ J m^{-3} K^{-2}; $\alpha_{17} = \alpha/10^{17}$ W m^{-3} K^{-2}; $\chi_{10} = \chi_{2T}/10$ cm^2/s, and $F_{100} = F_{\rm abs}/100$ mJ/cm^2. It is assumed that $\chi_{2T} \sim 10$ cm^2/s because an estimate based on molecular-kinetic theory gives $\chi \sim (1/3)lv_{\rm F} = 20$ cm^2/s for the electron mean free path $l = 3$ nm and Fermi velocity $v_{\rm F} = 2000$ km/s.

The values of thermal conductivity κ_{2T} can exceed the values of κ_{1T} in one-temperature (1T) states by more than an order of magnitude [7, 9, 11]. For this reason and on account of the fact that $\tau_T = t_{\rm eq} \gg \tau_L$, depth d_T (2) considerably exceeds skin depth δ. We can write the energy conservation law taking into account the change in the thickness of the heated layer during the time of 2T relaxation: $(E_i)_{\max} d_T \approx (E_e)_{\max}\delta \approx F_{\rm abs}$. Substituting these equations into relations (1) and (2) and assuming that $\delta = 15$ nm, we obtain

$$t_{\rm eq}[\text{pc}] \approx 4\frac{\gamma_{100}^{1/3}}{\alpha_{17}^{2/3}\chi_{10}^{1/3}} F_{100}^{1/3},$$

$$d_T[\text{nm}] \approx 65\frac{\gamma_{100}^{1/6}\chi_{10}^{1/3}}{\alpha_{17}^{1/3}} F_{100}^{1/6}.$$

These relations give an idea, first, of the characteristic scales of the hot layer and, second, of the extent to which indeterminacy in coefficients γ, α, and κ affects the electron–ion relaxation rate and thickness d_T of the heated layer. Assuming that $d_{\rm crat} \sim d_T$, we can estimate the depth $d_{\rm crat}$ of the crater above the ablation threshold.

In cases where laser radiation is acting on a metal, situations are possible for which $t_{\rm eq} < \tau_L < t_s$. Then 2T states do not appear, and time τ_T is equal to pulse duration τ_L. In this case, heating depth $d_T \sim \sqrt{\chi_{1T}\tau_L}$ is slightly smaller than depth (2): $\chi_{1T} \sim 1$ cm^2/s.

What are the remarkable features of supersonic heating ($d_T/\tau_T > c_s$)? Why are hydrodynamic effects especially significant for fast heating? As a matter of fact, in cases of supersonic heating, the substance has no time to expand in accordance with growing internal energy, which increases due to absorption of energy from an external source. This means that we are dealing with isochoric heating: $\rho = \rho^o$, where ρ^o is the density of the substance under normal conditions [4, 12–18]. The pressure in the layer being heated increases in proportion to the absorbed energy. For a fixed density $\rho = \rho^o$, the pressure is of the order of internal energy increment ΔE per unit volume because the Grüneisen parameter is on the order of unity. An increase in pressure p (as compared to the initial value $p = 0$) sets the substance in motion on the sound time scale t_s. The velocities of motion u are of the order of $p/z \sim \Delta E/z$ where $z = \rho c_s$ is the acoustic impedance of the medium. The energy increments typical of the conditions considered here are of the order of 1 eV/atom, the pressure is of the order of 10 GPa, and velocities $u \approx 0.4$ km/s. Conversely, slow heating ($\tau_T \gg t_s$) increases the pressure only slightly; therefore, velocities of condensed matter in this case are low ($u \ll \Delta E/z$).

Isochoric heating and thermomechanical factors do not only appear when an optical USLP is acting on metals. For an optical photon and a metal, skin depth $\delta \sim 10$–30 nm is small. For this reason, it is 2T thermal conductivity κ_{2T} and electron–ion heat transfer coefficient α [5, 7, 9] and not δ that determine scales d_T and τ_T (see relation (2)). In weakly absorbing media (e.g., in semiconductors with a band gap larger than photon energy or even in polymers [19]), thickness d_T is equal to the radiation absorption depth $d_{\rm att}$. For values of $d_{\rm att}$ of the order of a few micrometers, the boundary between the supersonic and subsonic regimes is at the heating pulse durations τ_L of the order of a nanosecond.[2] Thermal conductivity effects are usually insignificant at the hydrodynamic stage. A one-dimensional approximation cannot be used if radius R_L of the laser beam is on the order of or smaller than absorption length $d_{\rm att}$ (see the example with a polymer [19]). Other conditions being identical, the ablation threshold in absorbed fluence in joules per square centimeters increases approximately in proportion to depth $d_{\rm att}$ because to overcome the strength of the material, a required energy density ΔE per unit volume should be created. In the case of the thremofluctuational mechanism of nucleation, the threshold value ΔE decreases slowly (logarithmically) with increasing depth $d_{\rm att}$ due an increase in the volume in which nucleation takes place. The increase in the volume elevates the preexponential factor in the expression for the nucleation rate. This remark concerns the dependence of the threshold fluence on $d_{\rm att}$. Strain rate $\dot{V}/V \sim (u/c_s)/t_s = u/d_{\rm att}$ also decreases with increasing $d_{\rm att}$.

For lasers operating in the range of hard ultraviolet radiation or soft X-rays, the radiation frequency exceeds the plasma frequency. Therefore, the skin layer is absent, reflection is small, and absorption of photons mainly takes place in interband transitions. It is important that in the mechanism of absorption of hard photons, the strong difference between metals

---

[2] Here, we are speaking of intensities below the optical breakdown threshold. In the case of breakdown, the concentration of free electrons changes jumpwise. Accordingly, absorption depth $d_{\rm att}$ strongly decreases.

(without a gap in the energy spectrum in the conduction band) on the one hand and semiconductors and insulators (for which the gap exists) on the other hand disappears. In the case of hard photons, optical breakdown does not take place. During optical breakdown, length d_{att} sharply decreases with the development of the breakdown. In the case of illumination by hard radiation, absorption length d_{att} can only increase with increasing photon flux (for this purpose, extremal intensities are required [20, 21]). This increase is associated with a decrease in the number of electrons in a certain inner electron shell due to ionization [20, 21] (hollow ions). In this shell, predominant absorption of photons with a preset energy takes place.

The fundamental difference between a metal and a nonmetal is distinctive for optical photons (optical breakdown of semiconductors and insulators). In contract to the case of an optical laser and metals, in which the absorption depth is determined by the skin layer, absorption depth d_{att} (and, hence d_T) in the case of hard radiation sharply changes from values of the order of 10 nm to ~1 μm [22, 23] depending on the frequency of the hard photon relative to the edges of bands of inner electron shells (see examples given in [24, 25] for metals and silicon). Accordingly, together with heating depth, the thresholds and structure of residual damages of irradiated spot change sharply [24, 25]. Other examples of isochoric heating and thermomechanical effects correspond to bombardment by electron beams [26] or ion beams [27]. In this case, the values of d_{att} considerably exceed heating depth d_T (50–140 nm) by optical USLPs due to the large path lengths for high-energy particles. In these cases, the heating is supersonic if the pulse duration is limited to a value on the order of nanoseconds (if d_{att} is on the order of a micrometer) and microseconds for d_{att} on the order of 1 mm.

We considered above the physics of action of laser radiation on homogeneous targets, with emphasis laid on the thermomechanical ablation. The discussion was devoted to the determination of conditions for the thermomechanical regime in an extremely wide class of effects including, first, the action of short and long pulses; second, lasers with soft and hard photons, and third, metals, semiconductors, and insulators. We have also considered cases when ablation is one-dimensional and when 1D approximation is inapplicable.

In the case of thin films analyzed in this study, the situation changes from the case of homogeneous targets. Here, we assume that a film is thin if its thickness d_f is smaller than thickness d_T of the heated layer on the irradiated surface of the homogeneous target. To explain experiments performed in [28–33], we consider the thermomechanical ablation of thin films deposited on a dielectric substrate in the case of optical lasers. There are two peculiarities associated with thin films. First, there is the strong nonuniformity of heating in the film–substrate system due to the low thermal conductivity of the substrate as compared to the thermal conductivity of the metal. Therefore, almost the entire amount of heat applied to the metal remains in it over time intervals on the order of 100 ps and longer (these time intervals strongly exceed the acoustic scale $t_s \sim 10$ ps for films of thickness $d_f \sim 10$–100 nm). Second, there is the nonuniformity of the target tensile strength in the film–substrate system, for which the contact between the film and the substrate is the weak point due to limited adhesion.

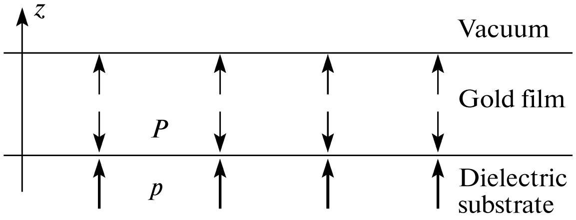

Fig. 1. Repulsion of film from substrate after isochoric heating of film by USLPs. Isochoric heating elevates pressure P in the gold film. Isochoric heating means that pressure increases rapidly as compared to hydrodynamic time d_f/c_s. Counterpressure p of the substrate imparts momentum to film in direction of z axis through film–substrate dynamic contact. If adhesive force is insufficient to balance the momentum gained by film, film is separated from substrate.

The thermomechanical ablation threshold F_a in a homogeneous metal target exposed to optical USLPs is two–three times higher than the melting threshold F_{m} [5, 34]. A surface layer of melt of thickness d_{m} of the order of thermal scale d_T is formed at threshold F_a and above it. For $F > F_a$, a rupture of metal takes place within the melt layer. In the case of films, the situation changes. A film clings to glass due to adhesion. The film separates from glass if the stress exceeds the limiting adhesion stress. As a rule, the maximal adhesion stress is substantially smaller than the ultimate stress in the bulk of the metal. In this case, the spalling threshold of the film from glass is below the melting threshold for the film; i.e., under the action of USLPs, even film that has not melted splits from glass if the stresses exceed the adhesion threshold. Spallation occurs not in the bulk of the film, but along the contact with the substrate (Fig. 1).

This study intends to explain phenomena observed in experiments [1, 28–33]. In these experiments, USLPs illuminate gold films of thickness $d_f \sim 20$–70 nm, which were deposited on dielectric substrates. As can be seen in the photographs from [1, 28–33], the observed phenomena occur due to the combination of hydrodynamic effects and surface tension. The solution to the problem proposed below is based on the division of the problem into two (initial and capillary) stages. At the initial stage, the film is accelerated along the normal to the substrate plane. Acceleration of the film is due to the counterpressure of the substrate (see Fig. 1). The counterpressure appears as the response of

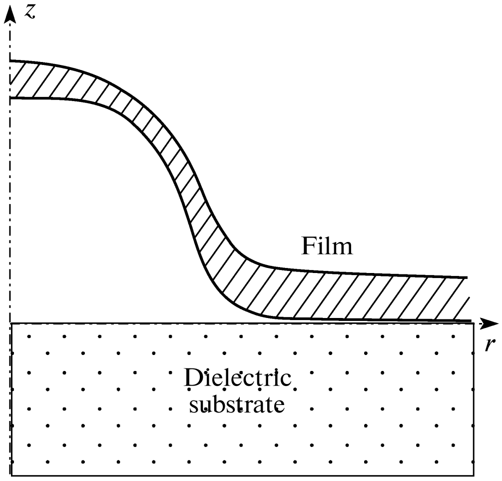

Fig. 2. Spallation and blistering of the film after action of a USLP. If maximal intensity of the USLP is at beam axis (e.g., in the Gaussian intensity distribution), detached film assumes cupola shape. For low energy supplied to heating spot, surface tension stops the upward motion of cupola along z axis and returns film back to substrate. At elevated energies, cupola spalls and flies upwards, leaving a hole in film on substrate. Figure shows symmetric half of pattern. Symmetry axis is z axis.

the substrate to the pressure of the film on the substrate. The duration of the acceleration stage is determined by hydrodynamic time $d_f/c_s \sim 10$ ps of the dynamic contact of the film with the substrate during and after the action of USLPs. The initial stage ends when the film is separated from the substrate.

To describe experiments [28–33], we must take into account the effect of surface tension. The capillary stage takes place if the film is melted and its velocity after the separation from the substrate is not too high. The scale of capillary velocities can be determined from a comparison of surface energy and kinetic energy:

$$\pi R_L^2 \sigma \sim \pi R_L^2 \rho^o d_f v_\sigma^2/2,$$

where R_L is the radius of the USLP beam, σ is the surface tension of the liquid metal, $\rho^o = 19.3$ g/cm^3 is the initial density of the gold film, and d_f is the initial film thickness. For typical values of parameters $R_L \sim 1$ μm, $\sigma \sim 10^3$ erg/cm^2, and $d_f \sim 50$ nm, we obtain $v_\sigma \sim$ 50 m/s. The heated spot on the film surface has its maximal temperature at the center because we consider USLPs with the maximal intensity to be on the beam axis. Thus the velocity distribution over the heated spot has the highest value at the center. In this case, the separated film assumes the shape of a cupola with the shell formed from the substance of the separated film (Fig. 2). The duration of the capillary stage can be estimated as $t_\sigma \sim R_L/v_\sigma \sim 10$ ns. It can be seen that the durations of the initial and capillary stages differ by three orders of magnitude.

The short time of the interaction of the film with the substrate (about 10 ps) as compared to the capillary time (about 10 ns) makes it possible to considerably simplify the complicated 3D problem, including the hydrodynamics of motion of the substrate and the film. With such a simplified approach, the problem is divided into two stages. At the first stage, we analyze the hydrodynamics of the film together with the substrate. We consider the absorption of the USLPs, the heating and relaxation of the electron subsystem, the thermal expansion of the film, the generation of a shock wave (SW) in the substrate, and the spallation of the film from the substrate. At this stage, the problem is solved in a one-dimensional (1D) approximation because the USLP beam diameter exceeds the film thickness by at least an order of magnitude ($d_f \sim$ 10–100 nm, while $R_L \sim 1$ μm and larger). In Section 2, the initial velocities of the local center of mass of the film and the local temperature are calculated as functions of the local value of absorbed laser energy $F_{\mathrm{abs}}(x, y)$ [J/cm^2], where x and y are the coordinates in the plane of the substrate surface (see Figs. 1 and 2). The second stage begins after the separation of the film from the substrate. The detachment region on the surface of the substrate has the shape of a spot bounded by a contour. In Section 3, the dynamics of the film fixed at the contour under the action of surface tension is described.

Experiments [1, 28–33] are directly related to future technologies. In these experiments, the formation of nanocupolas and nanojets is observed, which will widely be used in microelectronics, medicine, and nanoplasmonics [1, 2]. At present, three models have been proposed for explaining this important effect. In the first model, molecular-dynamics (MD) methods are employed to consider spallation of film from an absolutely rigid substrate [1]. Although this assumption (the rigidity of the substrate) considerably simplifies the problem,[3] it cannot be accepted. It will be shown below (see Section 2) that the presence of a deformable substrate reduces velocity v_z of separation of the film by 5–7 times. Low velocities $v_z \sim v_\sigma$ are required for the capillary effects (Section 3) to be manifested (nanojets cannot exist without them). In the formulation with the rigid substrate, velocity v_z can be reduced only by decreasing absorbed energy F_{abs}. However, in this case we operate below the melting threshold, and capillary effects disappear. It is necessary to observe the subtle balance between velocities $v_z \sim v_\sigma$ and melting. High velocities at a high temperature are required. It is shown in this study that this can be attained if the film expands into the "soft" substrate at the initial stage.[4]

---

[3] Because it eliminates the hydrodynamics of the substrate.

[4] "Soft" substrate means that its acoustic impedance is small compared to film impedance. In the case of a rigid substrate, the inverse situation takes place.

The second model [2] is limited to analysis of the dynamics of the film prior to its melting. In such a formulation, it is unclear how high-intensity mass fluxes to the axial region are formed (z axis in Fig. 2). However, it is these fluxes that are responsible for the jet formation at the vertex of a nanocupola (Section 3).

In the third model [33], the analysis of the near-surface dynamics of spallation of the film and its subsequent flight is replaced by the analysis of the Kuramoto–Sivashinsky (KS) phenomenological equation. This equation was used earlier by some authors for describing the formation of chaotic structures under laser action. Jet formation is attributed to the peculiarity of the KS equation [33]. In an approach based on the KS equation, the entire film dynamics is localized on the substrate (neither film detachment nor hollow expanding bump is considered). In this study, we combine the analysis of film separation (Section 2) with the capillary theory (Section 3). This allows us to describe even such a specific effect as the formation of the counterjet (see Fig. 22 below). This effect has been discovered recently (see Fig. 7 in [28]).

2. LASER IRRADIATION OF A FILM ON A SUBSTRATE

The laser energy absorption in the fluence range of interest ($F_{\rm abs} \sim 10$–100 mJ/cm^2) under isochoric heating produces pressures $\sim F_{\rm abs}/d_f = 10F_{10}/d_{10}$ (GPa) in the film, where $F_{10} = F_{\rm abs}/10$ [mJ/cm^2] and $d_{10} = d_f/10$ [nm]. Pressures with such amplitudes appear behind the detonation front of chemical explosives. It can be stated that the laser transforms the metal of the film into an explosive with pressures on the order of 10 GPa and temperatures $T \sim 1000$ K (T [K] $\sim 4000F_{10}/d_{10}$). Let us consider the expansion of such an "explosive" on the substrate surface (impact against the substrate and bounce from it). The distribution of the absorbed energy density $F_{\rm abs}$ is uniform over the film surface; see Fig. 1 (1D formulation of the problem). We must find the velocity $v_z(F_{\rm abs})$ of the center of mass of the film after its rebound from the insulator. The dielectric substrate is usually made of glass.[5]

In Section 2.1, we will describe a 2T thermodynamic model and the hydrodynamic equations used in this study. In Section 2.2, we will describe how thermal processes occur, because it is an increase in the internal energy that sets the substance in motion. We will study the absorption of laser radiation energy, electron heating, the propagation of heat over the electron subsystem, and electron–ion relaxation owing to which the lattice temperature increases and melting takes place. In section 2.3, we will give the description of the process of film spallation under uniform irradiation over the film surface (1D problem). In Section 3, the 3D spallation of film subjected to nonuniform irradiation is considered.

2.1. *Hydrodynamic Equations and a Thermodynamic Model*

The 1D motion of a film is described by the following two-temperature (2T) hydrodynamic equations:

$$\rho(z^o, t)\frac{\partial z(z^o, t)}{\partial z^o} = \rho^o, \quad \frac{\partial z(z^o, t)}{\partial t} = u(z^o, t), \tag{3}$$

$$\rho^o\frac{\partial u}{\partial t} = \frac{\partial P(z^o, t)}{\partial z^o}, \quad P = P_i + P_e, \tag{4}$$

$$\rho^o\left(\frac{E_e}{\rho}\right)_t = -q' - \frac{\rho^o}{\rho}\alpha(T_e - T_i) + \frac{\rho^o}{\rho}Q - P_e\frac{\partial u}{\partial z^o}, \tag{5}$$

$$\rho^o\frac{\partial(E_i/\rho)}{\partial t} = \frac{\rho^o}{\rho}\alpha(T_e - T_i) - P_i\frac{\partial u}{\partial z^o}, \tag{6}$$

where

$$Q = \frac{F_{\rm abs}}{\sqrt{\pi}\tau_L\delta}\exp\left(-\frac{t^2}{\tau_L^2}\right)\exp\left(-\frac{|z - z_g|}{\delta}\right),$$

$$(\ldots)_t \equiv \frac{\partial}{\partial t}, \quad q' \equiv \frac{\partial q}{\partial z^o}, \quad q = -\frac{\rho\kappa}{\rho^o}\frac{\partial T_e}{\partial z^o}.$$

The z axis is perpendicular to the plane of the film and substrate (see Fig. 1). We are using Lagrangian coordinate z^o. Prior to the action of USLPs, Lagrangian coordinate z^o coincides with the Euler coordinate z: $z^o \equiv z(z^o, t = -\infty)$. Function $z(z^o, t)$ defines the trajectory of a fixed material (Lagrangian) particle. In the 1D formulation, this is a plane moving along the z axis with velocity u. In this formulation, velocities perpendicular to the z axis are equal to zero. Equations (3) correspond to the conservation of mass and the kinematics of motion. The mass per unit area, $d\sigma_S = \rho^o dz^o$, which is pressed between the planes $z^o + dz^o$ and z^o, is constant. The dynamic equation has the form (4)—the difference of forces between planes $z^o + dz^o$ and z^o determines the acceleration of mass $d\sigma_S$.

The energy equations are written separately for the electron subsystem (Eq. (5)) and the ion subsystem (Eq. (6)) [6]. We disregard the thermal conductivity of glass in the time scale under consideration. In Eqs. (5) and (6), in addition to the thermal terms, the hydrodynamic terms associated with work $P\,dV$ in each subsystem are taken into account. These additions plus the hydrodynamic terms distinguish the hydrodynamic 2T system (3)–(6) from the 2T energy equations in the pioneering work [6].

It can be seen that time is measured from the peak of USLP intensity (formula for the source of Q). The spatiotemporal distribution of the absorbed energy is determined by function Q; the USLP duration is τ_L, and the absorption depth is equal to the skin depth δ.

---

[5] In [33], a CaF$_2$ substrate was used.

The dissipation of the electromagnetic wave energy occurs inside the metal near the film boundary. In the case of laser-induced forward transfer (LIFT) [1], in the formula for Q we take for z_g the glass–gold interface, because the laser beam passes through the substrate. In the case of laser-induced backward transfer (LIBT), we take for z_g the interface between the gold film and vacuum, because the laser beam passes through the vacuum gap (see Fig. 1).

Equations (3)–(6) of the 2T hydrodynamics are supplemented with the thermodynamic model of 2T states of condensed medium and with the model describing the most important kinetic coefficients (thermal conductivity κ and electron–ion heat-transfer coefficient α). In this study, in solving system (3)–(6), we take the 2T thermodynamic state equation (2T-EOS, equation of state) in the same form as in [35]; namely, 2T-EOS is represented by the sum of the ion and electron contributions; accordingly, free energy is given by

$$F(\rho, T_i, T_e) = F_i(\rho, T_i, T_e) + F_e(\rho, T_i, T_e). \qquad (7)$$

A number of approaches have been developed to calculating the electron contribution, from the Fermi and Thomas–Fermi models to quantum calculations based on density functional theory (DFT) [8, 9, 36–51]. Electron correction F_e to the one-temperature (1T, $T_e = T_i$) EOS has been taken into account for more than fifty years. This correction becomes significant at high temperatures [52] (see also [36, 37]). Earlier, correction F_e was calculated in the Fermi approximation. The approach in which electrons are described as an ideal gas (this forms the essence of the Fermi approximation) was extended to the 2T situation also [40, 41]. Modern studies are based on DFT simulation [8, 9, 35, 39, 42, 43, 45, 46, 48–51].

In this study, we are using a combination of the wide-range EOS [36, 37, 53, 54] and DFT computations [35]. Our DFT computations are in good agreement with the wide-range EOS over “cold” curves for metals [5, 35, 55, 56]. In connection with experiments [1, 28–33] on gold films, we are interested in the range of states with densities from the gas to the solid phase and with ion temperatures T_i up to a few kilokelvins and electron temperatures T_e up to a few electronvolts. In this range of states and for a fixed density ρ, we disregard the effects of (i) ion temperature T_i on the electron spectrum and (ii) electron temperature T_e on the elastic constants (electrons possess the Fermi energies, and the addition of a few electronvolts does not change the situation significantly [38]).[6] Under these two assumptions, we can write instead of expression (7) for the chosen range of states the approximate expression

$$F(\rho, T_i, T_e) = F_i(\rho, T_i, T_e) + F_e(\rho, T_e). \qquad (8)$$

Here, the dependence of function F_e on argument T_i is omitted in accordance with the first assumption. Function $F_i(\rho, T_i, T_e)$ weakly depends on the electron temperature (second assumption). Therefore, in function $F_i(\rho, T_i, T_e)$ in Eq. (8), we set $T_e = T_i = T$. The sum

$$F(\rho, T, T) = F_i(\rho, T, T) + \tilde{F}_e(\rho, T)$$

is used for calculating the wide-range 1T-EOS [36, 37, 53, 54].[7] In this case, the electron contribution $\tilde{F}_e(\rho, T)$ is calculated using an approximation close to the ideal gas approximation. To take into account the electron contribution refined here, we subtract function $\tilde{F}_e(\rho, T)$, which gives

$$F_i(\rho, T_i, T_i) = F(\rho, T_i, T_i) - \tilde{F}_e(\rho, T_i).$$

Thus, notation $F_i(\rho, T_i, T_i)$ in Eq. (8) indicates the 1T-EOS with the subtracted electron contribution. It should be noted that at temperatures T_i up to a few kilokelvins, electron contribution $\tilde{F}_e(\rho, T_i)$ is small, compared to ion contribution $F_i(\rho, T_i, T_i)$.

In approximation (8) adopted here, electron contribution F_e is independent of ion temperature T_i ($T_i \approx$ 2–5 kK). For this reason, this contribution can be calculated at zero ion temperature $T_i = 0$ (cold lattice). Accordingly, the electron one-particle spectrum of gold at $T_e = 0$ was calculated for the cold lattice using the DFT approach. Analogously to [8], this spectrum was used for determining electron energy E_e. The electron energy approximated used in the present study has the form

$$E_e = 17.513 \times 10^{-10}\left(\frac{1-\mathrm{tn}}{2} + 1.4\frac{1+\mathrm{tn}}{2}\right)T_e^2, \qquad (9)$$
$$\mathrm{tn} = \frac{2}{\pi}\arctan\frac{T_e - 3500}{700},$$

where E_e is given in kilojoules per gram and T_e is measured in kelvins. Approximation (9) reproduces the increase in the electron heat capacity upon an increase in temperature T_e due to excitation of d electrons. The electron pressure was calculated by the formula $P_e = (2/3)E_e\rho$. In the above approximation, addition F_e has the meaning of the electron thermal contribution to the Mie–Grüneisen equation.

For solving system (3)–(6), electron–ion heat transfer coefficient α and thermal conductivity κ are required. The former coefficient was borrowed from [7–9]. The thermal conductivity of gold in the 2T conditions was calculated by the formula

$$\kappa = \frac{1}{3}\frac{C_e v^2}{\nu},$$

---

[6] The second assumption is not applicable to semiconductors and insulators because it rules out athermal melting [57]. In addition, it is well known that gold strength noticeably increases upon a substantial increase in T_e [39, 46]. In the approximation used here, this effect has to be disregarded.

[7] In [36, 37, 53, 54], notation $F(\rho, T)$ is used instead of $F(\rho, T, T)$.

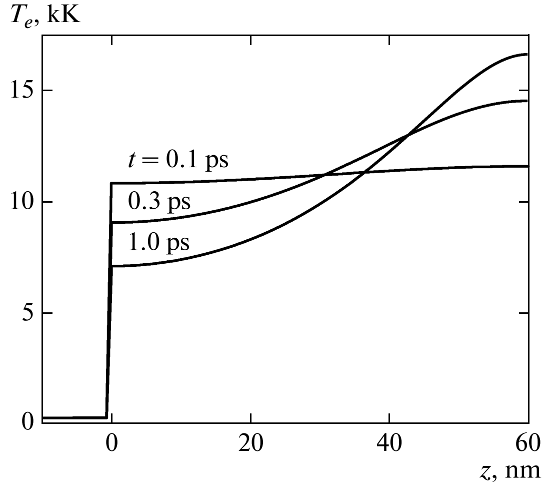

Fig. 3. Propagation of thermal wave and rapid leveling out of electron temperature T_e over film of thickness d_f = 60 nm. Absorbed energy F_{abs} = 40 mJ/cm^2. Point z = 0 corresponds to position of glass–gold contact prior to arrival of USLP at contact with vacuum z = 60 nm. Glass is on left, and gold is on right relative to z = 0. USLP illuminates film from right (from vacuum). Time t is measured from USLP peak. USLP duration is τ_L = 100 fs, skin depth is δ = 15 nm.

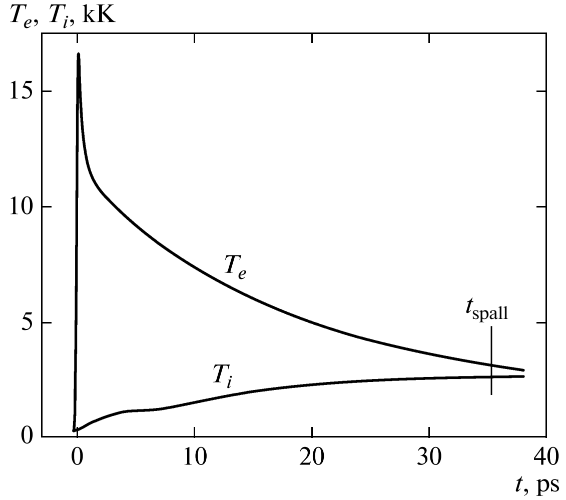

Fig. 4. Leveling out of electron T_e (z^o = 60 nm, t) and ion T_i(z^o = 60 nm, t) temperature due to electron–ion relaxation; τ_L = 100 fs, δ = 15 nm. Temperature curves correspond to interface between gold and vacuum. USLP energy is absorbed in skin layer at this boundary. Maximum T_e = 16.7 kK is attained at instant t = 0.11 ps. Initial temperature of gold and glass is 300 K. At $t > 1$ ps, the variation of T_e along normal to film is small (see text). This means that spatial profile $T_i(z, t)$ is approximately uniform along normal to film. At instant t_{spall}, film is detached from substrate.

where $C_e = \rho dE_e/dT_e$ is the heat capacity per unit volume, quantity E_e is defined by formula (9), $v^2 = v_F^2 + 3k_BT_e/m_e$, $m_e v_F^2/2$ = 5.5 eV is the Fermi energy E_F; E_F/k_B = 64 kK, and $E_F/\hbar$ = 8.4 fs^{-1}. Frequency ν is equal to the sum of frequencies $\nu_{ei} + \nu_{ee}$ of the electron–ion and electron–electron collisions. We assumed that $\nu_{ee} = (E_F/\hbar)(k_BT_e/E_F)^2$ [58]. Frequency ν_{ei} was determined from the resistivity using reference data [59]. It is ν_{ei} [s^{-1}] = $1.2 \times 10^{11} T_i(\rho^o/\rho)^{1.3}$ in the solid phase and ν_{ei} [s^{-1}] = $(0.34 + 2.7 \times 10^{-4} T_i)(\rho^o/\rho)^{1.3} \times 10^{15}$ in the liquid phase; here, ion temperature T_i is measured in kelvins and ρ^o = 19.3 g/cm^3 is the density of gold under normal conditions. Factor $(\rho^o/\rho)^{1.3}$ approximates the initial segment of conductivity fall upon a decrease in density [60]. Since our hydrodynamic code is based on wide-range multiphase EOS, we know the instantaneous phase composition at each Lagrangian particle. In the melting layer, frequency ν_{ei} was calculated using the formulas for the solid and liquid phases taking into account the volume fraction of phases in the two-phase mixture.

2.2. Thermal Processes

There are three thermal processes: (i) laser energy absorption in the gold skin layer of thickness of about 15 nm for the optical laser systems used with a photon energy of 1–1.5 eV; (ii) transfer of the absorbed energy to the bulk of the film by flux q in Eq. (5) due to electron thermal conductivity; and (iii) electron–ion temperature relaxation equalizing electron and ion temperatures, which is described by the term $\alpha(T_e - T_i)$. We disregard the thermal conductivity of the dielectric substrate on the time scales under investigation. For this reason, the thermal effects are localized in the gold film. In the 2T conditions, the thermal conductivity is high, films [1, 28–33] are thin, and the film is heated extremely rapidly. Accordingly, detailed knowledge of the thermal conductivity is not very significant for interpreting experiments [1, 28–33].[8] The values of electron–ion heat transfer coefficient α and electron pressure P_e turn out to be more important because relaxation lasts over an appreciable time interval.

Figure 3 shows a typical example of numerous calculations in various variants. The system of equations (3)–(6) of the 2T thermohydrodynamics is solved numerically. It is well known [5] that at the 2T stage in homogeneous bulk targets, an electron thermal wave propagates with an ultrasonic velocity—a "quasi-homogeneous" heating of the layer of thickness d_T takes place. In the case of thin films ($d_f < d_T$),

---

[8] Thermal conductivity is important for determining heating depth d_T and the thermomechanical ablation threshold for bulk targets.

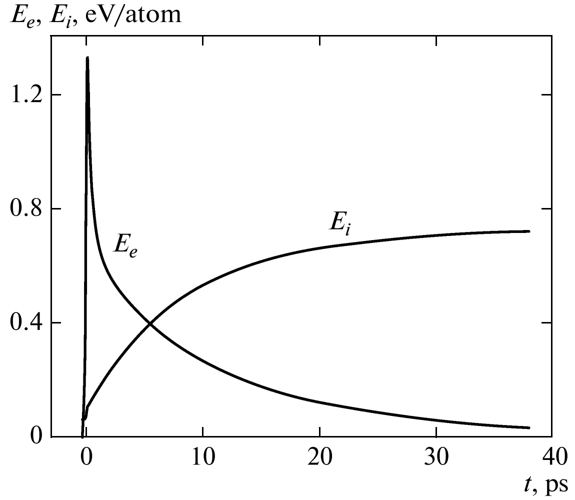

Fig. 5. Energy pumping from electrons to ions at $T_e > T_i$. It can be seen that less than 22% of total energy $E_e + E_i$ is left in electrons at $t > 15$ ps. Time dependences of energies are given for Lagrangian particle at gold–vacuum interface, $z^o = 60$ nm. Computation is made with parameters from Figs. 3 and 4.

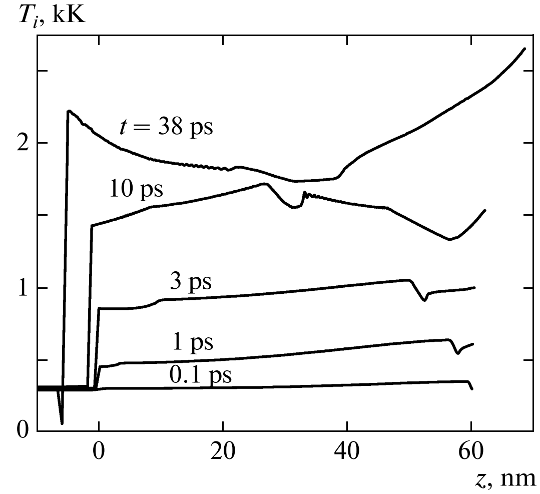

Fig. 6. Heating of ions by bulk source (hot electrons) due to term $T_e - T_i$ in Eqs. (5) and (6). Parameters are same as in Figs. 3–5.

this effect leads to a rapid leveling out of the electron temperature over the space (see Fig. 3). Even by the end of the first picosecond, the temperature difference

$$\Delta T_e(t) = T_e(z^o = 60\text{ nm}, t) - T_e(z^o = 0, t)$$

at the surfaces of the film decreases to 7% of the average temperature of the boundaries

$$\bar{T}_e(t) = \frac{1}{2}[T_e(z^o = 60\text{ nm}, t) + T_e(z^o = 0, t)],$$

$\Delta T_e(t = 3\text{ ps})/\bar{T}_e(t = 3\text{ ps}) < 10^{-3}$. Narrow peaks in Figs. 4 and 5 are due to the rapid heat transfer from the skin layer of thickness $\delta = 15$ nm to the film of thickness $d_f = 60$ nm.

The process of equalization of the electron (T_e) and ion (T_i) temperatures is illustrated in Fig. 4. This process is associated with coefficient α in energy equations (5) and (6). For thin gold films, the leveling out of temperature $T_e(z, t)$ takes a much shorter time than electron–ion temperature relaxation (see Figs. 3 and 4). It can be seen from Fig. 4 that temperature relaxation continues for tens of picoseconds and does not terminate by instant $t_{\text{spall}} = 35.3$ ps of film spall from glass (dynamic effects and film spallation will be considered in the next section). Actual relaxation occurs faster (Fig. 5). It is associated with the transfer of absorbed energy F_{abs} (which is stored in the electron subsystem) from electrons to ions. Even at instant $t = 5.4$ ps, these energies become equal, although the electrons are hotter by 8 times (cf. Figs. 4 and 5). Naturally, this is due to the small electron heat capacity, as compared to $3k_B$ at temperatures T_e of a few kilokelvins.

Figure 6 illustrates the heating of the ion subsystem. The bulk source of heat corresponds to the term $\alpha(T_e - T_i)$ in Eq. (6). After the rapid leveling out of temperature T_e (see Fig. 3), the power of the heating source is approximately uniform at coordinate z. The temperature profile $T_i(z, t)$ is also affected by the term $P_i\text{div}u$ associated with work $P\,dV$ and with the hydrodynamic motion.

In approximation (8) adopted above, we disregarded the effect of electron excitation on the elastic constants. This means that melting curve $T_m(P)$ weakly depends on electron temperature T_e. In addition, we carried out hydrodynamic computations using the thermodynamic state equation. Consequently, our calculations do not describe the kinetics of melting. This is a considerable drawback if we are speaking of the region near the melting threshold. Spinodal $T_s(P)$ of an overheated crystal lies 25–40% higher than the melting curve [61]: $T_s(P) \approx (1.25–1.4)T_{\text{m}}(P)$. For $F_{\text{abs}} = 40$ mJ/cm^2 (see Figs. 3–6), the ion temperature increases to values of about 2 kK (see Fig. 6). Temperatures of about 2 kK correspond to the neighborhood of spinodal $T_s(P)$. At such overheating amplitudes, kinetic effects are insignificant.

For high velocities of propagation of the melting layer over the film material, a two-phase spatial region with a mixture of the solid and liquid phases appears. The local concentration of phases in the mixture gradually changes with time. High rates of spatial expansion of the region of transition of the crystal to the melt are due to the high velocities of propagation of the electron wave in the case of USLPs (see Fig. 3). Accordingly, the electron temperature rapidly levels out over the film thickness. Therefore, the ion subsystem is heated almost uniformly over space (see Fig. 6). Consequently, the phase composition of the

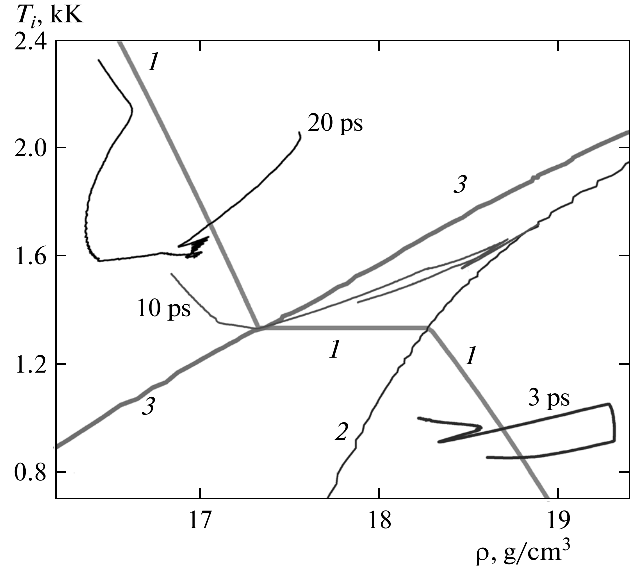

Fig. 7. Evolution of instantaneous ion temperature spatial profile $T_i[\rho(x, t), t]$ under action of bulk heating of ion subsystem: (*1*) binodal; (*2*) solidus; (*3*) liquidus. Evolution proceeds from the solid to melt. Profile corresponds to instants $t = 3$, 10, and 20 ps. At instants close to 10 ps, intersection of zone of crystal–liquid two-phase mixture takes place. The phase curves are described in text. Parameters of action and films are same as in Figs. 3–6.

film material varies almost uniformly with time. The situation is complicated because the extension of gold in expansion waves leads to the emergence of regions in which the substance intersects the binodal and passes into a metastable state.

Figure 7 shows the phase diagram of gold in accordance with wide-range EOS [36, 37, 53, 54]. The binodal (curve *1*) separates the two-phase region containing vapor and the condensed phase. The horizontal segment with $T_i = 1337$ K on the binodal corresponds to the triple point. The solidus (curve *2*) separates the crystal from the two-phase mixture of the solid and liquid phases. The liquidus (curve *3*) is the upper boundary of the two-phase mixture of the solid and liquid phases in equilibrium melting. Three $T_i(\rho, t)$ profiles of the $\rho(z^o, t)$ and $T_i(z^o, t)$ distributions over the gold film thickness are superimposed on the binodal. The instantaneous profiles are individual curves on which temperature T_i on the phase plane in Fig. 7 rises from the lower curve to the middle one and from the middle curve to the upper one. Higher temperatures in Fig. 7 are at the top. On a specific instantaneous profile, hotter points in temperature T_i are located closer to the interface between gold and vacuum (see Fig. 6). This is due to the fact that in the variant corresponding to Figs. 3–7, the film is heated by the laser from the side of vacuum.

At instant $t \approx 10$ ps, the $T_i(\rho, t)$ profiles intersect the two-phase solidus–liquidus strip. This means that the entire gold film melts. It is interesting that the expansion waves meet precisely on the interval of times corresponding to melting. The above arguments correspond to the case when $F_{\mathrm{abs}} = 40$ mJ/cm^2. Two expansion waves [14, 16] propagating over the film from the interfaces with vacuum and glass meet approximately at the middle of the film. Pay attention to the dip corresponding to the middle of the film in Fig. 6 on the profile with $t = 10$ ps. Together with the decrease in temperature T_i towards the film edges, this dip indicates that two expansion waves have met.

The profiles contain segments on which the substance is in the stretched state with a negative ion pressure $P_i < 0$. First, this is due to the fact that the always positive electron pressure stretches the condensed phase in the expansion wave (see the discussion in [55, 56, 62]). Second, the partial pressures (P_e, P_i) and the total pressure ($P = P_e + P_i$) change due to energy transfer from electrons to ions. Therefore, expansion waves are not strictly self-similar waves. On segments with $P_i < 0$, the substance passes to the metastable state. The extension amplitude is insufficient for the rupture of the condensed phase on our time scales. Segments of profiles with $P_i < 0$ are located under binodal *1* in Fig. 7. It should be noted that in the given variant of the wide-range EOS, solidus *2* and liquidus *3* are continued into the metastable region [18].

The profile with $t = 20$ ps in Fig. 7 corresponds to the stage at which the region of extension approaches the contact interface between the film (gold) and substrate (glass). For this reason, the more heated region corresponding to gold outside the contact region lies under the binodal. Only the region near the contact remains in the compressed state. Then the expansion wave propagating from vacuum reaches the contact interface, on which the pressure decreases to zero. If we disregard the cohesion between gold and glass, the film spalls from the substrate at instant t_{spall}, when pressure $P_c(t)$ at the contact vanishes (see Section 2.3, devoted to dynamic effects).

Why does the spallation of the film occur at the instant when $P_c(t_{\mathrm{spall}}) = 0$? The reason is quite simple. If spallation did not take place, function $P_c(t)$ would become negative: $P_c(t) < 0$ for $t > t_{\mathrm{spall}}$. However, by hypothesis, the cohesion stress P_{coh} of gold on glass is small. Let us consider situations with finite values of the mechanical strength of the contact. Let function $\Delta v(P_{\mathrm{coh}})$ describe the dependence of the velocity of separation of the boundaries of glass and gold at spall instant t_{spall} determined by the equation $-P_c(t_{\mathrm{spall}}) = P_{\mathrm{coh}}$. Note that velocity $\Delta v(P_{\mathrm{coh}})$ vanishes for $P_{\mathrm{coh}} = 0$ and increases with P_{coh}. Therefore, for a low cohesion stress of the film on the substrate ($P_{\mathrm{coh}} \approx 0$), the gap between the boundaries of the film and substrate at $t > t_{\mathrm{spall}}$ increases slowly.

The case of a film with $d_f = 60$ nm and $F_{\mathrm{abs}} = 40$ mJ/cm^2 is analyzed in Figs. 3–7. The film spalls from glass at instant $t_{\mathrm{spall}} = 35$ ps (see table). After spallation, the film flies in the molten state (see Fig. 7). Let us find out how the value of the absorbed energy affects

Phase composition, spall time t_{spall}, and velocity v_{cm} of the center of mass of the film of thickness $d_f = 60$ nm after spallation; $n^o = 6 \times 10^{22}$ cm^{-3} is the initial concentration of gold atoms

F_{abs}, mJ/cm^2	10	20	30	40
$F_{\text{abs}}/d_f n^o$, eV/atom	0.17	0.35	0.52	0.69
t_{spall}, ps	25	28.5	37	35
$T(t_{\text{spall}})$, kK	0.9	1.337	1.7	2.4
Amount of liquid phase, %	0	20	100	100
v_{cm}, m/s	12.6	25	53	70

the phase state for other values of F_{abs}. The table contains spall instants t_{spall} disregarding the mechanical strength of the glass–film contact. Apart from values of t_{spall}, the center-of-mass velocities v_{cm} of the film after its spallation from glass are also given in the table. These data will be required in Section 2.3.

The table is necessary for determining the melting threshold above which the film flies after spallation in a completely molten state. The table can be used instead of the curves shown in Fig. 7 for $F_{\text{abs}} =$ 40 mJ/cm^2 in the cases with other values of F_{abs}. It can be seen from the table that fluence $F_{\text{abs}} = 10$ mJ/cm^2 is insufficient for melting. In this case, at the stage of the dynamic interaction of the film with glass ($t < t_{\text{spall}}$) and after spallation ($t > t_{\text{spall}}$), the film remains in the solid state. Therefore, the fraction of the liquid phase is zero. The amount of the liquid phase is given in the table. The action of USLPs heats the metal to 0.9 kK. The initial temperature is 0.3 kK. Temperature increment ΔT can be easily estimated by writing the energy balance equation $d_f C \Delta T = F_{\text{abs}}$. For $d_f = 60$ nm, $C \approx 3k_B n^o$, $n^o \approx 6 \times 10^{22}$ cm^{-3}, and $F_{\text{abs}} = 10$ mJ/cm^2, we obtain $\Delta T = 0.67$ kK. This estimate is approximately 10% higher than the true temperature difference because the energy stored in the compression wave in glass is disregarded. At instant $t_{\text{spall}} = 25$ ps, the kinetic energy of the film amounts to 0.3% of energy F_{abs}. The kinetic energy $(1/2)\rho^o d_f v_{\text{cm}}^2$ of directional motion of the center of mass at instant $t_{\text{spall}} = 25$ ps amounts to 0.18% of energy F_{abs}.

For $F_{\text{abs}} = 20$ mJ/cm^2, calculations using the equilibrium equation of state show that gold attains the temperature of the triple point even before its spallation (see table). In calculations with the equilibrium equation of state, melting occurs faster than in the case when the kinetics of melting is taken into account. This effect is significant if the overheating is small and does not reach the spinodal of the heated solid phase. As mentioned above, the temperature on the spinodal is 25–40% higher [61] than the temperature on the melting curve. The variant with $F_{\text{abs}} =$ 20 mJ/cm^2 corresponds to small overheating. For this reason, gold at the spall instant is in the state of an overheated solid phase. Partial melting occurs later, during the flight. The melting threshold lies between 20 and 30 mJ/cm^2. For $F_{\text{abs}} = 30$ mJ/cm^2, gold melts even before spallation from glass. At this energy, the instantaneous distribution of the phase composition over the film intersects the two-phase melt–crystal region in the time interval from 9 to 21 ps. The process of intersection of the two-phase strip at $F_{\text{abs}} =$ 40 mJ/cm^2 is illustrated in Fig. 7.

In our formulation, one boundary of the film is vacuum and the other boundary is glass. Analysis of the dynamics of a free film with vacuum at both boundaries was carried out in [63, 64] (see also [65]). In these publications, the melting and ablation thresholds were determined as functions of parameter $F_{\text{abs}}/d_f n^o$ given in the table. The data in the table are in conformity with the results obtained in [63, 64] for the melting threshold.

2.3. Dynamic Behavior

The reason for the hydrodynamic motion of the film and substrate is the thermal expansion of gold. That is why we analyze dynamic phenomena after thermal effects. In this section, we consider the formation and propagation of two expansion waves in the film and the propagation of a compression wave in glass. Two interesting new effects were discovered. First, there is the "wake" of the superfast increase and decrease of electron pressure P_e. The wake is formed at the ultrashort stage of the superfast increase and decrease in pressure P_e during the action of a USLP of extremely short duration $\tau_L \sim 0.1$ ps. After its formation, the wake travels from the boundary with the vacuum to the bulk of the film and then to the glass.

Second, the refraction and reflection of the expansion wave propagating from the gold–vacuum interface at the film–glass contact with a high ratio of acoustical impedances is also of interest. The above wake splits into two (transmitted and reflected) wakes during refraction and reflection of the extension wave. The process of reflection considerably affects the accumulation of momentum of the film during the dynamic interaction between gold and glass. The acquired momentum determines the center-of-mass velocity v_{cm} of the film (see table) after it spalls from the glass. The shape of the cupola formed by the separated film depends on the energy distribution $F_{\text{abs}}(x, y)$ over the illuminated spot and function $v_{\text{cm}}(F_{\text{abs}})$ (see Fig. 2). The main goal of 1D hydrodynamic analysis is the determination of temperature $T(F_{\text{abs}})$ and velocity $v_{\text{cm}}(F_{\text{abs}})$ of the spalled film. This information is required for solving the 3D problem of film flight. The 3D problem is considered in Section 3.

Figure 8 shows the A, B, and C profiles of the rarefaction wave propagating from the interface with vacuum. In a condensed medium, the rarefaction wave

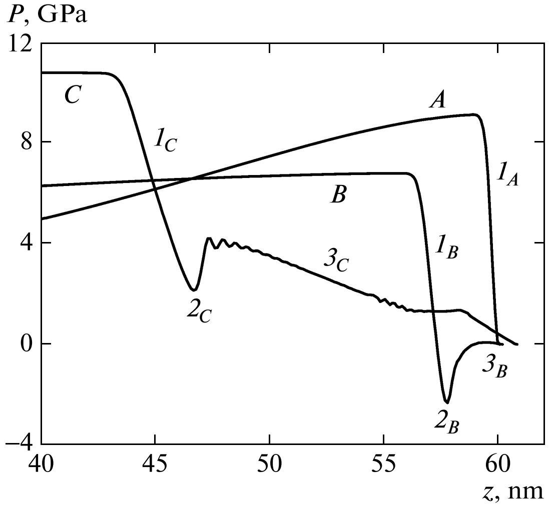

Fig. 8. Propagation of the expansion wave from the vacuum boundary to the bulk of the film (from right to left). Profiles *A*, *B*, and *C* correspond to instants $t = 0.1$, 1, and 5 ps. Parameters of the USLP and of film are same as in Figs. 3–7.

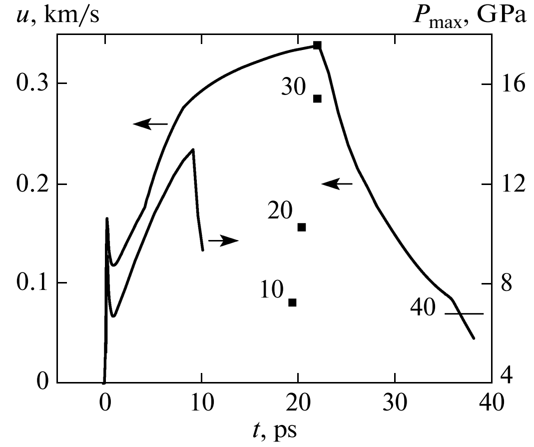

Fig. 9. Time evolution of velocity u of the gold–vacuum interface and maximal total pressure P_{max} for F_{abs} = 40 mJ/cm^2. The values of $P_{max}(t)$ are determined by the maximal value at the instantaneous velocity profile corresponding to instant t. Squares correspond to instant and magnitude of maximal velocity of vacuum boundary. The numbers 40, 30, 20, and 10 give values of energy F_{abs}. Horizontal segment with the number 40 gives center-of-mass velocity v_{cm} from table. Pay attention to the large ratio of velocity of boundary (square 40) and velocity v_{cm} (segment 40).

has a form differing from its form in a gaseous medium [4, 12, 13, 66]. This is due to the fact that in contrast to gas, a condensed medium exhibits a finite resistance to stretching, and the rarefaction wave contains a segment with decreasing pressure and density as well as the segment with a constant flow (plateau). The pressure on the plateau is equal to the pressure of the surrounding medium. During expansion into vacuum, the pressure on the plateau is zero, and the substance on the plateau is located on the binodal shown in Fig. 7. The corresponding profiles in Fig. 8 contain segments *1* of sharp decrease in pressure and plateaus *3*. The smaller the wave amplitude, the more exact the description of the flow by the expression of linear acoustics, and the shorter and steeper the segment *1* of pressure drop. Due to nonlinear effects, the steepness of segment *1* decreases with time because the velocity of sound is greater under higher pressure. The measure of nonlinearity is the ratio of the pressure amplitude to bulk modulus K ($K = 180$ GPa for gold). At 0.1 ps, the plateau on the profile is not yet formed (see Fig. 8). In the given situation, the pressure in the bulk of the film varies with time due to the electron–ion heat transfer. For this reason, instead of a regular plateau with zero pressure gradient and zero pressure, we have segment *3* of “quasi-plateau” with a small pressure gradient and a low pressure. The exact plateau and self-similar segment *1* correspond to a steady-state homogeneous situation [4, 12, 13, 66].

Pay attention to a peculiar dip *2* on the pressure profiles in Fig. 8. It is located at the kink between segment *1* and the quasi-plateau and moves along with this kink. This means that the dip runs over the characteristics of the rarefaction wave and that it has been formed at the interface with vacuum at instant $t \approx 0$. The propagation of the dip from right to the left can also be traced from the local drops of ion temperature T_i in Fig. 6, which shows that at instant $t = 10$ ps, the dip reaches the middle of the film.

The dip resembles in appearance the “Z-wave” consisting of a compression segment with $P > 0$ and an extension segment with $P < 0$. Such a wave is typical. It is always formed from thermomechanical action on a thick target if its thickness is larger than d_T. The x, t diagram in [67, 68] (see Fig. 1 in [67] and [68]) shows that segments with $P > 0$ and $P < 0$ propagate in pairs. Pressure profiles with a pair of segments with $P > 0$ and $P < 0$ are given in [65, 69, 70]. The formation of the Z-wave is explained in [71]. The Z-wave is formed due to the spatial inhomogeneity of the rapid (supersonic, isochoric) heating of the substance at the boundary of the target. The inhomogeneity is characterized by thickness d_T of the heated layer. Accordingly, the segments of the Z-wave with positive and negative pressures have a length of the order of d_T.

However, the thickness of the dip (length of the interval along the z axis occupied by the dip) in our situation is much smaller than the inhomogeneity scale d_T, which exceeds the film thickness $d_f = 60$ nm. To explain the reasons for the formation of the dip, let us consider the time dependences of the velocity of the interface with the vacuum and the total pressure maximum. These dependences are shown in Fig. 9. It can be seen that the total pressure exhibits a short and sharp peak, as well as the boundary velocity peak connected with it. The same peak can be seen on the curves for the electron temperature and energy in

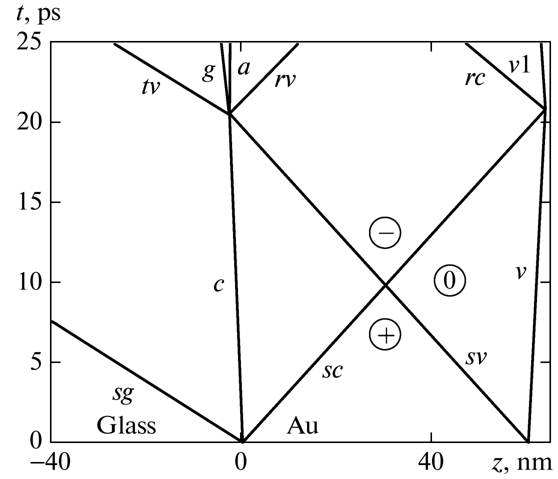

Fig. 10. Propagation of two counterpropagating expansion waves *sc* and *sv* over gold film. Wave *sc* runs from the contact and *sv* from vacuum boundary *v*, *v*1. Leading edge of compression wave front in glass is denoted by *sg*.

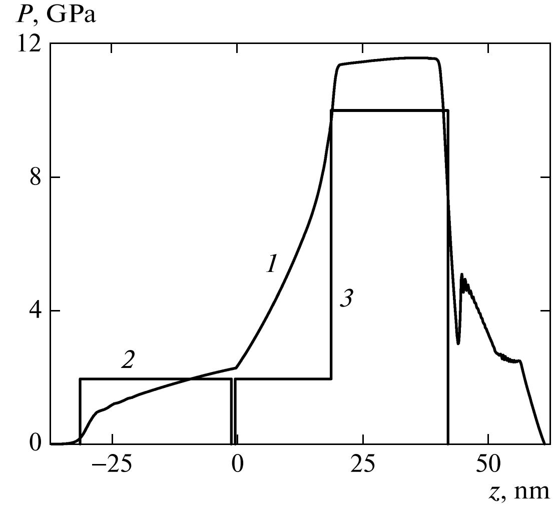

Fig. 11. Comparison of numerical (curve *1*) and linear analytic (broken lines *2* and *3*) solutions. Instant $t = 6$ ps; $F_{\text{abs}} = 40$ mJ/cm^2, $d_f = 60$ nm, $\tau_L = 100$ fs.

Figs. 4 and 5. The emergence of the peak of total pressure $P = P_i + P_e$ is due to the high rate of heat release in the skin layer due to extremely short time of the laser pulse action ($\tau_L = 100$ fs). Then the electron contribution to the pressure sharply decreases due to rapid spatial transfer of heat from the skin layer. This effect is illustrated above in Fig. 3; it can be seen that leveling out of electron temperature T_e over the film takes only one picosecond.

The decrease in the values of T_e and P_e due to the electron–ion heat transfer lasts much longer than their decrease due to heat conduction and, hence, is not responsible for the formation of the dip. It can be seen from Fig. 9 that after the first sharp peak at $t \approx 0$, the total pressure increases over time intervals determined by the electron–ion heat transfer. This increase is due to the fact that the ion Grüneisen parameter $\Gamma_i \approx 2$ is larger than its electron counterpart $\Gamma_e \approx 1$ [35]. Accordingly, for a small change in the specific volume, the total pressure increases as the energy is transferred from the electron subsystem to the ion subsystem.

The extension of the substance at the boundary appears due to the fact that the velocity of the boundary was initially high and later decreased. For this reason, deeper layers decelerate the rapidly flying layer at the boundary. Therefore, the increase and decrease in pressure (sharp peak in Fig. 9) lead to the formation of a layer with extension and negative pressure. This situation corresponds to profile *B* and dip 2_B in Fig. 8. Then the pressure begins to increase, and the boundary is accelerated relatively slowly (as compared to the peak at $t \approx 0$; see Fig. 9). The conditions for stretching the material at the boundary disappear. However, the wake of the dip created at the early stage ($t \approx 0$) passes to the extension wave and propagates over the characteristics (hence, is preserved). In this case, the pressure in the wake becomes positive due to the increase in the total pressure and the acceleration of the boundary (see the example with profile *C* and dip 2_C in Fig. 8). In this case, the shape of the dip is preserved. Its width slowly increases due to the dependence of the velocity of sound on the amplitude (nonlinear effect).

The peak, dip, and its wake in the expansion wave running to the left in Figs. 6 and 8 were discovered owing to the fact that system (3)–(6) was solved numerically with the small spatial step of 0.02–0.1 nm. The width of the dip is 1–2 nm. It is determined by a scale of the order of $c_s\tau_L$. Such a fine effect could hardly be detected in molecular dynamics because for $\tau_L = 0.1$ ps, the dip width is comparable with atomic spacing.

In addition to the above rarefaction wave propagating from the vacuum interface, an rarefaction wave propagating over the film from the glass–gold contact also exists. The rarefaction wave propagates into the gold and the compression wave propagates into the glass. The *z*, *t* diagram in Fig. 10 shows the motion of the waves schematically. The acoustic impedance of glass $Z_g = 0.9 \times 10^6$ g/cm^2 s is smaller than the acoustic impedance of gold $Z_a = 5.9 \times 10^6$ g/(cm^2 s). The analytic acoustic solution in the linear approximation is given in [72]. The numerical solution analyzed here is much more informative than the analytic solution. These solutions are compared in Fig. 11. In hydrodynamic 2T calculations, aluminum is chosen as the substrate because its equation of state is familiar and it is close to glass in density and sound velocity; however, the acoustic impedance of aluminum ($Z = 1.4 \times 10^6$ g/(cm^2 s)) is 1.5 times higher. This circumstance (passage to aluminum) increases the center-of-mass velocity v_{cm} by 1.4 times and decreases the velocity of the contact by 8%. The analytic solution given in

Fig. 11 was calculated by solution of a Riemann problem at vacuum and glass boundaries. It is assumed that for $F_{\text{abs}} = 40$ mJ/cm^2, a USLP instantaneously produces pressure $P_o = 10$ GPa, which is uniform over the film (P_o is the time-averaged pressure from Fig. 9). We neglect here the leveling out of temperature T_e over the film due to heat conduction (cf. Fig. 3) as well as the change in the total pressure due to energy transfer to the ion subsystem and the difference between the electron and ion Grüneisen parameters (see Fig. 9).

Under these assumptions, the analytic solution consists of a set of two constant pressures shown in Fig. 11. The positions and values of the constant pressures vary with time. This occurs in accordance with the diagram in Fig. 10. Let us briefly describe the analytic solution to grasp the qualitative features of the numerical solution. Over time intervals $0 < t < t_s/2$ ($t_s = d_f/c_s \approx 20$ ps, $c_s = 3.05$ km/s is the velocity of sound in gold under standard conditions), we obtain the following three values of pressure from left to right in the analytic solution: $p_c = P_oZ/(Z + Z_a)$, P_o, and 0 (three plateaus in Fig. 11). The values of pressure P_o on the middle segment and $P = 0$ on the right segment are marked by symbols "+" and "0" in Fig. 10. The pressure boundaries of rectangles (the density jump at the contact also exists) move with the velocity of sound in the corresponding medium. The velocity of contact is $u_c = P_o/(Z + Z_a)$; the velocity of the interface with the vacuum is P_o/Z_a.

On the time interval $t_s/2 < t < t_s$, we have the following values of three pressures: p_c,

$$P_{\text{neg}} = -P_o + p_c = -P_oZ_a/(Z + Z_a) \tag{10}$$

and 0. The pressures on the second and third segments are marked by symbols "–" and "0" in Fig. 10. It can be seen that large tensile stresses (negative pressure) appear in the triangular region marked by the minus sign in Fig. 10. The extension layer (minus sign) expands with time. The expansion towards the contact continues until the sound wave sv in Fig. 10 reaches the film boundary c. Coordinates z, t of the point of intersection of trajectories sv and c in Fig. 10 are given by

$$\begin{gathered}\frac{z_{sp}}{d_f} = -\left[\frac{K}{P_o}\left(1 + \frac{Z}{Z_a}\right) - 1\right]^{-1}, \\ t_{sp} = \frac{t_s}{1 - (P_o/K)/(1 + Z/Z_a)} \approx t_s.\end{gathered} \tag{11}$$

It can be seen that in the linear regime $P_o \ll K$, displacement z_{sp} is small as compared to film thickness d_f (see Fig. 10). The measure of nonlinearity is the ratio P_o/K of the pressure to the bulk modulus for gold, while the measure of symmetry in the film expansion is the ratio of the impedances. In the case of symmetric expansion, when both boundaries of the film are boundaries with vacuum, we have $Z/Z_a = 0$ and $v_{\text{cm}} = 0$.

It should be emphasized that the case of the stationary contact corresponds to an infinitely large impedance of glass; accordingly, $Z/Z_a = \infty$. The problem was considered with such a formulation in [1, 2]. In this case, the type of the dynamic interaction of the film with the contact changes qualitatively. Instead of rarefaction wave sc, which begins to propagate into glass to the left and to gold to the right at instant $t/t_s \approx 0$ (see Fig. 10), the substance at the contact remains at rest with an invariable density until rarefaction wave sv emitted from the interface with vacuum at instant $t \approx 0$ arrives at the contact. This affects the flow in the whole (e.g., the velocity of the interface with vacuum in Fig. 9 does not decrease at instant $t \approx t_s$ because this decrease is associated with the arrival of rarefaction wave sc from the contact). Velocity v_{cm} of the center of mass of the film after its separation from the glass turns out to be much higher than the values given in the table. This is due to the absence of the expansion towards the glass.

Let us return to the case when $Z \ll Z_a$, which is observed in experiments. At $t = t_{sp} + 0$, the expansion wave arrives at boundary c, and the extension of the contact between the film and the substrate begins. If we neglect the adhesion of gold to glass ($P_{\text{coh}} = 0$), the separation of the film from the substrate occurs at instant t_{spall} (spall instant). In Fig. 10, two divergent trajectories g and a appear after spallation. The hydrodynamic flow profile in this cases can be divided into five segments: (1) sg–tv, pressure is p_c, tv is the transmitted wave formed as a result of refraction of rarefaction wave sv at the impedance jump at contact c; (2) tv–g, pressure is zero; (3) a–rv, pressure is zero; (4) rv–rc, pressure P_{neg} (10) is negative; and (5) rc–$v1$, pressure is zero.

Let us return to the description of the numerical solution. Rarefaction waves sc and sv in Fig. 10 meet at the middle of the film at instant $t \approx t_s/2 \approx 10$ ps. The beginning of the sharp pressure drop (see Fig. 9) is associated with the meeting of waves sc and sv. After its encounter with wave sv, rarefaction wave sc continues its motion to interface v with vacuum. The sc wave reaches the vacuum interface at instant $t \approx t_s$. This instant separates segments v and $v1$ of the trajectory of the interface with vacuum, in which the velocity of the interface has different signs. At instant $t_s \approx 20$ ps, the velocity of the interface with vacuum begins to decrease (see Fig. 9). Approximately at the same instant $t \approx t_s$, expansion wave sv propagating from the vacuum interface reaches the contact (see Fig. 10).

The evolution of the profiles prior to the meeting of the sc and sv waves is illustrated in Fig. 12. The situation corresponds to simple evolution of the pressure jump decay between gold under pressure and glass in which the pressure is zero. The energy transfer to ions from bulk source $\alpha(T_e - T_i)$ in Eq. (6) increases total pressure P (see Fig. 9) due to the difference in the Grüneisen parameters. The electron–ion relaxation continued approximately for 5–15 ps (see Fig. 5) in energy and about 35 ps in temperature (see Fig. 4). The increase in pressure with time substantially

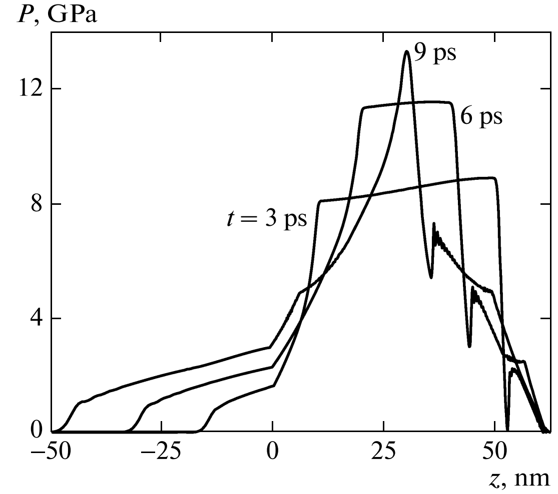

Fig. 12. Slow expansion of film and propagation of the compression wave into glass. Transformation of left (*sc*) and right (*sv*) expansion waves before their meeting approximately at middle of film. $F_{\text{abs}} = 40$ mJ/cm^2.

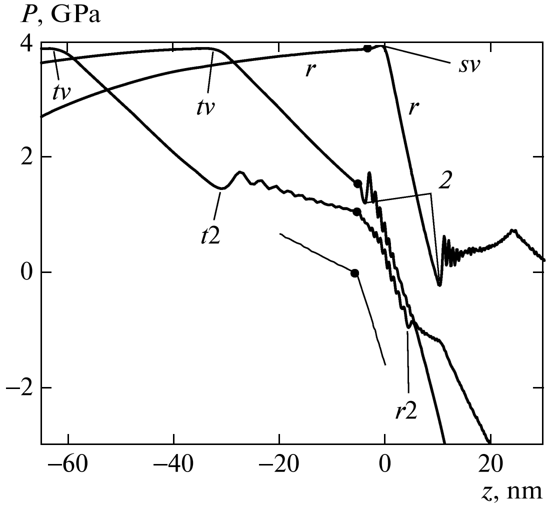

Fig. 13. Passage of steep segment *sv–2* and quasi-plateau of expansion wave propagating from interface with vacuum through glass–gold contact. Four profiles (from right to left) correspond to instants $t = 19$, 25, 30, and 35.3 ps. To simplify figure, only a piece near contact is left in profile at 35.3 ps. At instant 35.3 ps, pressure on contact decreases to zero, after which boundaries of glass and gold slowly diverge.

changes the numerical solution as compared to the analytic solution (see Fig. 11). In the regions containing the plateau on the right and left sides in the analytic solution, we observe the distributions of P increasing along the z axis. The increase in P in the direction to the high-pressure layer inside the gold film is due to the increase in P with time in the high-pressure layer. The kink of the gradient of P at contact c is associated with the density jump at the contact. The accelerations of particles on the left and on the right of the contact are identical, but the densities are different: the ratio of gradients of P is equal to the ratio of densities; i.e., the gradient in gold is steeper.

Let us consider the interaction of the sv wave with contact c. In linear acoustics, the interaction at $t_{sc} \approx$ 20 ps (11) instantaneously leads to spallation. In the actual situation, spallation occurs later; e.g., for $F_{\text{abs}} =$ 40 mJ/cm^2, we have $t_{\text{spall}} = 35$ ps (see table). This is due to blur of the wavefront and the existence of a quasi-plateau with a nonzero pressure (see Fig. 8), on which the wavefront is marked by digits *1* for three instants of time, and the quasi-plateau is denoted by digits *3*. In linear acoustics, the reflection $sv \longrightarrow c$ leads to the emergence of the tv wave transmitted to glass, a discontinuity with banks g and a, and reflected wave rv (see Fig. 10). The sv wave has two important acoustic characteristics. This is the sv characteristic running ahead and the characteristic at the kink between the front and the quasi-plateau (see Fig. 8). The characteristic at the kink is marked by digit the *2* in Fig. 8.

Figure 13 illustrates the passage of the sv wave through contact c for $F_{\text{abs}} = 40$ mJ/cm^2. The positions of contact c at instants of 19, 25, 30, and 35.3 ps are marked by circles. At 19 ps, the right rarefaction wave (see Fig. 12) reaches the contact. At this instant, characteristics sv and *2* of this wave are on the right of the contact. The kink of gradient ∇P still accelerates the contact. Characteristics sv and *2* border the steep segment of the expansion wave propagating from right to left from the interface with vacuum (see Fig. 12). Further, the characteristic sv crosses the contact and is transformed into a transmitted characteristic tv (see Fig. 13). At 25 ps, the characteristic *2* comes close to the contact. On the profile corresponding to 30 ps, the singularities associated with the transmitted characteristic *t2* and reflected characteristic *r2* are indicated. Characteristics *t2* and *r2* are generated by the characteristic *2*. When steep segment sv*–2* passes through the contact, pressure on it rapidly decreases. Therefore, the acceleration of the contact changes for its deceleration. Accordingly, gradient ∇P changes sign. However, the absolute value of the pressure gradient in gold is higher as before because the density of gold is higher than the density of glass.

Let us calculate velocity v_{cm} of the center of mass of the film after its spall from glass. Prior to the action of a USLP, the momentum of the film + glass system is zero. If the film has detached from the substrate, the total momentum is zero as before (we disregard the momentum of absorbed photons). However, the momentum of the film

$$i = \int_{z^o = 0}^{z^o = 60} \rho u dx$$

becomes a finite quantity given by

$$i = \int_{-\infty}^{t_{sp}} p_c(t)dt.$$

Therefore, velocity $v_{\rm cm} = i/m$ is determined by the pressure on the contact; here,

$$m = \int_{z^o = 0}^{z^o = 60} \rho dx = \rho^o d_f$$

is the mass of the film.

The integrand function $p_c(t)$ is shown in Fig. 14. In the linear case, the momentum and velocity are $p_c t_s$ and $v_{\rm cm} = (Z_g/Z_a)u_c$, where $u_c = P_o/(Z_g + Z_a)$. In the linear case, function $p_c(t)$ has a rectangular shape. This function is zero for $t > t_{sp} \approx t_s \approx 20$ ps (11) (see Figs. 10 and 11). In the actual situation, instead of the rectangle in Fig. 14, we have an increasing function with values decreasing after characteristic *sv* intersects the contact. The intersection occurs at instant $t_{sp} \approx 20$ ps. Between points *sc* and *2* in Fig. 14, pressure $p_c(t)$ decreases sharply. This segment corresponds to the passage of the steep segment *sv–2* of the rarefaction wave propagating from vacuum (see Figs. 11–13). Then the quasi-plateau of rarefaction wave *sv* arrives at the contact. This corresponds to the segment between points *2* and $t_{\rm spall}$. The value of $t_{\rm spall}$ for $F_{\rm abs}$ = 40 mJ/cm^2 is given in the table. As a result, the film acquires velocity $v_{\rm cm}$ given in the table. The curve in Fig. 14 resembles the curve for the velocity of the interface with vacuum in Fig. 9. However, the decrease in velocity in Fig. 9 is determined by the rarefaction wave propagating from the contact, whereas the pressure drop in Fig. 14 is determined by the rarefaction wave propagating from the interface with vacuum.

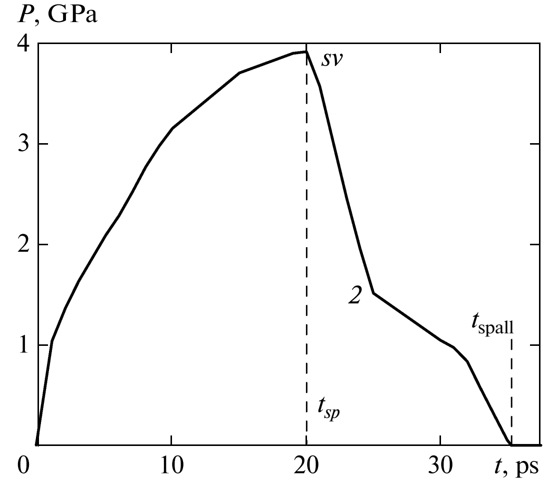

Fig. 14. Acceleration of center of mass of film due to pressure of glass on film via glass–gold contact. First, total pressure $P = P_e + P_i$ increases due to electron–ion relaxation. Then characteristic *sv* arrives at the contact, and pressure $p_c(t)$ begins to decrease rapidly (see also Fig. 13). $F_{\rm abs}$ = 40 mJ/cm^2.

3. BLISTERING OF THE FILM ON THE SUBSTRATE

3.1. Capillary Effects

The above computations based on the 1D hydrodynamic 2T code play an exceptional role. These computations clarify the mechanism of spallation of a metal film from the dielectric substrate and determine the initial velocity field $v_{\rm cm}(x, y) = v_{\rm cm}[F_{\rm abs}(x, y)]$. The code approximates system of equations (3)–(6). An important parameter is laser beam diameter R_L. This parameter is connected with non-one-dimensional effects considered in the present section. The intensity distribution in the direction perpendicular to the beam axis decreases with increasing distance from the beam axis. For the function approximating the intensity distribution in the plane perpendicular to the beam axis, we can take any cupola-shaped function (e.g., the Gaussian function). The intensity distribution over the film surface is proportional to $\exp(-x^2/R_L^2)$ in the case of the strip beam, $\exp(-r^2/R_L^2)$, $r^2 = x^2 + y^2$ for an axisymmetric beam, and $\exp[-(x^2 + y^2\cos^2\beta)/R_L^2]$ in the case of an axisymmetric beam incident on the target at angle β between the normal and the beam axis.

Let us consider the case where the film in the heating spot has melted under the action of a USLP. In this case, the surface tension of the hot melt affects the dynamics of the flight of the film after its spallation from glass. The surface tension coefficient is a fixed (invariable) function of the temperature of the liquid phase (Fig. 15). The same property (invariability) is exhibited by density ρ^o of gold under standard conditions. Therefore, it may appear that the effect of coefficient σ on the dynamics is determined by variable quantities R_L, d_f, and v_o (for v_o, we take the center-or-mass velocity of the film on the laser beam axis; see table).[9] However, radius R_L cannot be used as a parameter. The capillary scale of velocity v_σ can be determined by comparing the surface energy and the kinetic energy of the film:

$$2\sigma = \frac{\rho^o v_\sigma^2}{2} d_f, \quad v_\sigma^2 = \frac{4\sigma}{\rho^o d_f} \equiv \frac{4\sigma}{\mu_o}, \tag{12}$$

where μ_o [g/cm^2] = $\rho^o d_f$ is the surface density of the film before it starts moving. Radius R_L does not appear

---

[9] As mentioned in Section 1, the spallation of the film on the one hand and its flight on the other hand can be considered separately. Indeed, the time scales of these two processes differ by three orders of magnitude. The duration of the former process is $t_s \sim 10$ ps, while the duration of the latter process is $R_L/v_o \sim$ 10 ns; i.e., $R_L/v_o \gg t_s$.

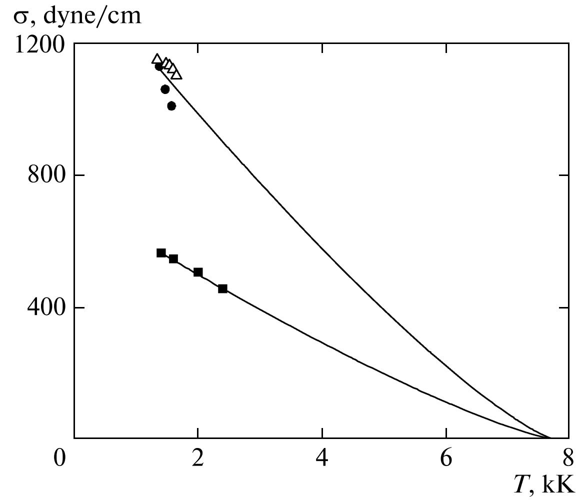

Fig. 15. Surface tension σ on a segment of vapor–liquid binodal (i.e., on boiling curve; see Appendix). Triangles and bullets correspond to experimental data from [73, 74]. Squares are values of σ according to gold potential [70] calculated in embedded atom model (EAM). Curves are approximations of form $\sigma(T) = \sigma_3[(1 - T/T_c)/(1 - T_3/T_c)]^{1.25}$ [75], $T_3 = 1.337$ kK and $T_c = 7.756$ kK are temperatures at triple and critical points, $\sigma_3 = \sigma(T_3)$. EAM potentials are known to give noticeably lower values of coefficient σ.

in parameter v_σ. Factor 2 appears in front of σ in the first relation in (12), because after spallation from glass, the film has two surfaces. Thus, if we disregard cooling due to heat conduction along the metal surface and freezing of the melt, the only dimensionless parameter controlling the motion is the dimensionless velocity

$$\hat{V}_o = v_o/v_\sigma. \tag{13}$$

If we disregard the rupture of the film (assuming that the film is infinitely stretchable), the surface tension always terminates the motion of the separating film and returns it to the substrate even when $\hat{V}_o \gg 1$ (13) if the kinetic energy at the initial stage dominates. The shape of the film on the substrate is shown in Fig. 2. Indeed, surface energy increases indefinitely with increasing film surface, while the kinetic energy is limited.

Then what is the role of parameter R_L, if it does not appear in the definition of parameter (13)? For a fixed value of $\hat{V}_o$ (13), the evolution of the swelling (“bumping”) (see Fig. 2) is the same in the dimensionless coordinates

$$\hat{x} = \frac{x}{R_L}, \quad \hat{y} = \frac{y}{R_L}, \quad \hat{z} = \frac{z}{R_L}, \quad \hat{t} = \frac{t}{R_L/v_\sigma}, \tag{14}$$

i.e., for identical parameters $\hat{V}_o$ at identical instants $\hat{t}$, the bump size is just proportional to R_L.

Let us write the equation of motion of the film in dimensionless form:

$$\frac{\partial^2\hat{r}}{\partial\hat{t}^2} = -C\frac{\partial\hat{z}}{\partial\hat{a}}, \quad \frac{\partial^2\hat{z}}{\partial\hat{t}^2} = C\frac{\partial\hat{r}}{\partial\hat{a}},$$
$$\hat{R} = \frac{k^3}{\hat{z}''\hat{r}' - \hat{r}''\hat{z}'}, \quad k = \sqrt{\hat{r}'^2 + \hat{z}'^2}, \tag{15}$$
$$\hat{r}' = \frac{\partial\hat{r}}{\partial\hat{a}}, \quad \hat{z}' = \frac{\partial\hat{z}}{\partial\hat{a}}, \quad C = \frac{1}{2}\left(\frac{\hat{r}}{\hat{a}\hat{R}} + \frac{\hat{z}'}{k\hat{a}}\right).$$

System of two equations (15) corresponds to the axisymmetric geometry. The z axis in Fig. 2 is the rotational axis and r is the cylindrical radius (i.e., distance $\hat{r} = r/R_L$ to the z axis). The film is assumed to be infinitely thin. Lagrangian coordinate a runs over the arc of the film ($\hat{a} = a/R_L$). Coordinate a is defined as the initial value of radius r at which a material particle of the film on the substrate was located before the film started moving. Before the motion begins, the surface of the substrate coincides with the plane $z = 0$.

In dimensional variables, system (15) has the form

$$\frac{\partial^2\xi}{\partial t^2} = -2\frac{\sigma}{\mu_o}\frac{r}{a}\frac{ds}{da}(R_{rz}^{-1} + R_t^{-1})\mathbf{n}, \tag{16}$$

where $\xi = \{r, z\}$ and

$$R_{rz} = \frac{s'^3}{z''r' - r''z'}$$

is the radius of curvature of the curve that forms the axisymmetric bulging surface of the film in Fig. 2 upon rotation about the z axis; $r' = \partial r/\partial a$. This planar curve lies in the rz plane. The second radius of curvature in Eq. (16),

$$R_t = \frac{r}{\cos\alpha} = \frac{rs'}{z'},$$

corresponds to the planar curve lying in the intersection of plane N and the surface of revolution; $\cos\alpha = dz/ds$, α is the angle between the z axis and the tangent to the film. This tangent lies in the rz plane. Plane N passes through the normal vector **n** to the film surface and the perpendicular to the rz plane. Radius R_t is equal to the distance from a point on the film to the z axis along normal **n**.

The term on the left-hand side of Eq. (16) is associated with the inertia force $(2\pi a\, da)\mu_o\ddot{\xi}$ of a ring of mass $(2\pi a\, da)\mu_o$, where $2\pi a\, da$ is the area of this ring on the substrate surface prior to the action of a USLP. The normal to the point with coordinates r, z on the film surface in Fig. 2 is directed outwards (to the bulge of the film) Accordingly, the pressure difference produced by the surface tension is directed inwards and decelerates the film. This corresponds to the minus sign on the right-hand side of Eq. (16). The term on the right-hand side contains the force $(2\pi r\, ds)p$ of capillary pressure p exerted on the ring of area $2\pi r\, ds$. Factor $(1/\mu_o)(r/a)s'$ on the right-hand side of Eq. (16) is formed by the mass (without 2π) $\mu_o a da$ and area (without 2π) $r\,ds$ of the ring. The flying film has two free surfaces; for this reason, factor 2 appears on the right-hand side of Eq. (16).

In the 2D case, system (15) assumes the form

$$\frac{\partial^2\hat{x}}{\partial\hat{t}^2} = -\frac{1}{2\hat{R}_p}\frac{\partial\hat{z}}{\partial\hat{a}}, \quad \frac{\partial^2\hat{z}}{\partial\hat{t}^2} = \frac{1}{2\hat{R}_p}\frac{\partial\hat{x}}{\partial\hat{a}}, \tag{17}$$

$$\hat{R}_p = \frac{k^3}{\hat{z}''\hat{x}' - \hat{x}''\hat{z}'}, \quad k = \sqrt{\hat{x}'^2 + \hat{z}'^2}, \quad \hat{x}' = \frac{\partial\hat{x}}{\partial\hat{a}}.$$

In the planar geometry, the bulge has the shape of a strip along the y axis. Accordingly, curve $z(x, t)$ lies in the plane $y = \text{const}$. Instead of radius $r(a, t)$ of the cylinder, system (17) contains coordinate $x(a, t)$.

3.2. Results of Integration

The nonlinear system of partial differential equations (15) was solved numerically with initial and boundary conditions. The initial conditions have the form

$$r(a, t=-0) = a, \quad z(a, t=-0) = 0,$$
$$\frac{\partial r(a, t=-0) = 0}{\partial t} = 0, \tag{18}$$
$$\frac{\partial z(a, t=-0)}{\partial t} = \hat{V}_o v_\sigma \cos^2\frac{\pi a}{2R_L}.$$

These conditions distribute material particles uniformly over the substrate plane on segment $0 < a < R_L$ and specify the initial distribution of velocity $\partial z/\partial t$ directed normally to the substrate. As mentioned in Sections 2 and 3, we can disregard time intervals $t_s \sim$ 20 ps, over which the film is spalled from the substrate, as compared to time intervals $R_L/v_\sigma \sim 1$ [μm]/100[m/s] ~ 10 ns, during which the film moves over distances of the order of R_L. Therefore, time in conditions (18) is measured from instant $t = 0$. The problem of the action of a USLP has the boundary conditions

$$r(a = 0, t) = 0, \quad \partial z(a = 0, t)/\partial a = 0, \tag{19}$$

$$r(a = R_L, t) = R_L, \quad z(a = R_L, t) = 0, \tag{20}$$

which correspond to the central Lagrangian particle ($a = 0$) on the z axis and to a finite curvature of the film at the vertex (19). In addition, the outermost Lagrangian particle ($a = R_L$) is fixed at point $r = R_L$, $z = 0$ (20). Systems (15)–(17) are of the fourth order in time and of the fourth order in the coordinate. Therefore, eight initial and boundary conditions (18)–(20) are required for their solution.

Systems (15)–(17) were analyzed in recent publication [72]. In contrast to that publication, we present an important classification of solutions depending on the key parameter $\hat{V}_o$ (13), while in [17] several individual cases were considered, in which the "turn-over" of the solution takes place, and a droplet is generated at the top of the bulge. The inaccuracy of the result in [72] is corrected (expression (15) for parameter C must contain a factor of 1/2). In addition, new molecular-dynamics (MD) calculations in planar geometry corresponding to Eqs. (17) are carried out. Most importantly, we present for the first time the results of MD simulation in the axisymmetric geometry, which allows us to explain theoretically the origin of the recently detected effect of formation of a backward jet (see Fig. 7 in [28]).

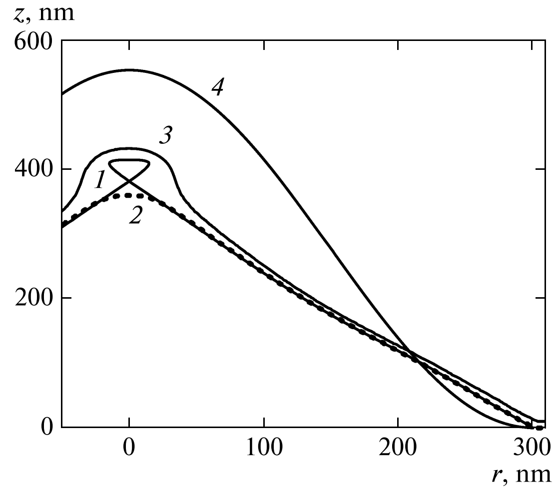

Fig. 16. Comparison of large-scale (0.2×10^9 particles) MD simulation and results of integration of system (15): (curve *1*) at instant $t = 1.846$ ns, $\hat{t} = 0.70954 \approx 0.71$; curves *2* and *3* are lower and upper boundaries of the film according to MD calculations. Parameters of calculation are given in text. Level $z = 0$ corresponds to substrate surface prior to the USLP action. For inertial curve *4*, $\sigma = 0$ (the film flies by inertia); the remaining parameters are same as in solution of system (15).

For small values of $\hat{V}_o \ll 1$ (13), the film returns to the substrate after the departure to a small distance from it. For this reason, a droplet at the top of the cupola has no time to be formed. The formation of the drop and jet at the top occurs when $\hat{V}_o = \hat{V}_{\text{cr}}$. Before writing the expression for $\hat{V}_{\text{cr}}$ for the planar and cylindrical geometries, let us analyze the case when $\hat{V}_o > \hat{V}_{\text{cr}}$. Comparison of MD simulations with the solution of system (15) in this case is illustrated in Fig. 16. The parameters of calculations are as follows. Axisymmetric laser action: $\hat{V}_o = 2.60177$ (13); $R_L = 300$ nm; $v_o = 300$ m/s; and $\mu_o = 1.64356 \times 10^{-5}$ g/cm^2. Prior to the action of the USLP, the film of an fcc gold crystal has a thickness of 23 lattice constants equal to 0.429434 nm under standard conditions ($p = 0$) for our EAM potential. In the MD simulation, the Langevin thermostat with zero flow velocity, which forces the bulge edge to stay on the substrate, permanently operates in the region bounded by a circle of radius $r = 300$ nm and a

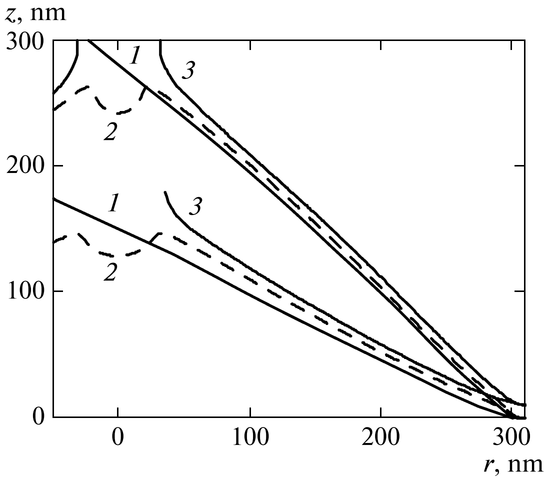

Fig. 17. Upper and lower groups of three curves corresponds to $t = 2.86$ and 3.81 ns, respectively. The zones of the central jet and counterjet are present. Film at indicated instants has passed through stop stage and moves back to substrate. Numbers on curves and parameters of problem are same as in Fig. 16. Concave part in central zone of the lower curve *2* corresponds to incipient counterjet.

620 × 620 nm square. In calculations, we used $191832512 \approx 200 \times 10^6$ atoms. The surface tension of 546 dyne/cm for system (15) was the same as in the MD simulation (see Appendix and Fig. 15). In the MD simulation, the temperature of the gold melt was 1600 K and the density was 16.55 g/cm^2; the substance is on the binodal in this case (see Appendix). After melting by the thermostat and before the beginning of motion, the film thickness was 9.9 nm. In the MD simulation, we assume that the substance is between the upper and lower boundaries of the film (see Fig. 16).

Comparison of MD data with the results obtained by numerical integration of system (15) shows good agreement between them even after the beginning of formation of a droplet at the top (see Fig. 16). In system (15), the droplet corresponds to a loop at the vertex. Figure 16 illustrates a late instant, before which capillary forces have considerably decelerated the cupola (cf. curves *1* and *4*). Satisfactory agreement between the MD simulation and calculation based on system (15) is preserved even over large time intervals, when the mass of the droplet becomes quite large (Fig. 17).

We are speaking of comparison of the film shapes (in the MD simulation and in accordance with Eqs. (15)) outside the central region where the jet (directed upwards) and the counterjet (directed downwards) are located. The computation (based on the solution of system (15)) gives values of 26% and 40% for the droplet mass at instants $t = 2.86$ ns and $t = 3.81$ ns, respectively. The curves in Fig. 17 correspond to these two instants. The percentage shows the ratio of the droplet mass to the total mass of the film inside the circle of radius R_L (see condition (20)). To determine the mass of the droplet from the solution of system (15), we must find point a_{drop} at which function $r(a, t)$ vanishes for the first time upon a variation of Lagrangian coordinate a from 1 to d_{drop}. At this point, self-intersection of the film on the z axis takes place. An example of self-intersection is given in Fig. 16 in the form of a loop at the top of the cone-shaped cupola. The shape of the film is specified by parametric functions $r(a, t)$ and $z(a, t)$, which are solutions to system (15). At instant $t = 1.846$ ns, corresponding to Fig. 16, the coordinate of the self-intersection point is $\hat{a}_{\text{drop}} = 0.2285391$, and the mass of the droplet (loop) divided by the total mass is $\pi\hat{a}^2_{\text{drop}}/\pi\hat{R}^2_L = 0.228539^2 = 5.22\%$. The value of a_{drop} determines the coordinate at which the curves of model (15) in Fig. 17 intersect the z axis.

Before the beginning of motion under the action of a USLP, the film was in contact with the z axis for $a = 0$. Lagrangian particle $a = 0$ is the only particle on the z axis after the beginning of motion and up to instant t_{drop} at which self-intersection takes place. In model (15), a nucleus of a drop appears at instant t_{drop} at the top of the cupola. Then the nucleus develops into a jet and a counterjet as follows from the MD simulation. At $t > t_{\text{drop}}$, the film covers the segment from the z axis to the point of attachment $r = R_L$ due to a decrease in the number of Lagrangian particles a: $a_{\text{drop}} < a < R_L$. Thus, due to the expansion of the cupola during its upward motion and due to loss of the substance to the droplet, the film is stretched. Accordingly, its thickness decreases. It should be noted that in the case illustrated in Fig. 17, ballooning turns over the motion towards the substrate. In this case, the accumulation of the substance in the droplet reduces the film thickness, while the reduction of the area of the lateral surface of the cupola produces the opposite effect.

Figure 18 shows the mass distribution over radius r. In model (15), we have

$$\begin{aligned} h &= \frac{\mu_o}{\rho}\frac{a/r(a, t)}{\partial s/\partial a}, \\ \Delta z &= \frac{\mu_o}{\rho}\frac{a/r(a, t)}{\partial r/\partial a}, \end{aligned} \qquad (21)$$

where h is the film thickness equal to distance between two points lying on the normal vector to the film surface, one of which belongs to the upper boundary of the film, and the other to its lower boundary; Δz is the difference in heights $z_{\text{high}}(r, t)$ and $z_{\text{low}}(r, t)$; μ_o is the mass per unit area of the film prior to the USLP action; and ρ is the density of gold in the film (at the melt temperature of 1.6 kK, this density is 16.55 g/cm^3). The above formulas follow from the mass conservation law $2\pi a\, da\mu_o = 2\pi r\, ds\rho h$. The film thickness sharply increases in the central zone (see Fig. 18), where the circular droplet is gradually trans-

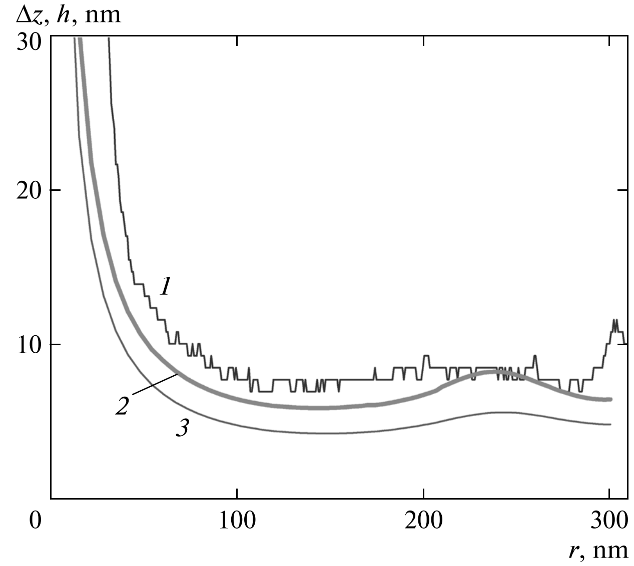

Fig. 18. Curves $\Delta z = z_{\mathrm{high}}(r, t) - z_{\mathrm{low}}(r, t)$ give the difference in heights of upper and lower surfaces along the z axis at instant $t = 2.86$ ns. Curve *1* corresponds to MD computation, and curve *2* corresponds to system (15). Film thickness h (curve *3*) is plotted in accordance with relation (21). Parameters are same as in Fig. 16.

formed (see Fig. 16) into a jet and a counterjet extended along the z axis.

The variation of the film thickness with time is illustrated in Fig. 19. It can be seen that the thickness increases towards the cupola axis $r = 0$. The cupola assumes a conical shape (see Figs. 16 and 17). The cone height (disregarding the jet) decreases from 0.4 to 0.15 μm over time interval 2–4 ns. The substance of the film flows with time to the central zone (the jet in this zone operates as a mass sink for the remaining part of the film). The flow is determined by the sign of deceleration (directed downwards to the substrate and to the z axis). As noted above, at the stage of the backward motion of the cupola to the substrate, the mass sink is acting in the direction of the decrease in the film thickness, while the cupola area decreases in the opposite direction.[10] On the segment of evolution depicted in Fig. 19, the mass of the central formation increases from 5 to 40% (see above). The cone area decreases thereby from 0.5 to 0.3 μm^2.

Apparently, the decrease in the cupola surface area slightly compensates the flow of the substance to the axial zone. Therefore, over a time interval of 2 ns (from $t = 1.846$ to 3.81 ns), the film thickness has changed insignificantly. However, the film thickness, compared to the initial value $h \approx 10$ nm, has decreased almost by half. By instant $t = 3.81$ ns, the minimum of the thickness has been displaced to the cone base (see Fig. 19). This probably means that if the film does not crystallize, the spall ring is closer to the substrate (cf. [33]). The liquid cupola detached from the substrate is gradually transformed during its flight from a complex formation to a spherical drop [72]. This process is controlled by dissipation of capillary oscillations. At instant $t = 3.81$ ns illustrated in Fig. 19, the minimal film thickness is approximately 4 nm. The rupture of the liquid film takes place when its thickness decreases to about 1 nm (3–4 atomic spacings). This conclusion follows from the analysis of nanobulging in planar geometry [72] and from the analysis of foaming and breakup of foam in molten metals [5, 55]. Capillary effects, nucleation processes, and foaming in the case of a large spot of heating ($R_L \sim 1$ μm) have much in common. Foaming of the melt and freezing of foam were assumed in [5, 55, 76–78] to be the mechanisms of formation of chaotic structures observed in experiments [79–81].

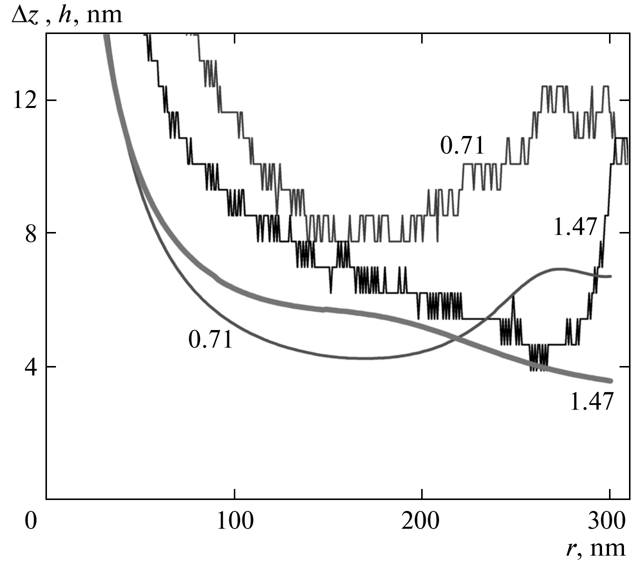

Fig. 19. Difference Δz (two upper step curves) from the MD computations and film thicknesses h in accordance with relation (21). Parameters are same as in Fig. 16. Differences Δz and thicknesses h are given at two instants $\hat{t} = 0.70954$ ($t = 1.846$ ns) and $\hat{t} = 1.46594$ ($t = 3.81403$ ns). Digits on curves give rounded values of dimensionless time $\hat{t}$ (14). Dependences $\Delta z(r)$ and $h(r)$ gradually converge (cf. pair Δz and h at instants $t = 1.8$ ns and $t = 3.8$ ns). This is due to increase in cone angle with decreasing distance between film and substrate (see Figs. 16 and 17).

3.3. Jet and Counterjet

Figure 20 shows the kinematics of the ascent and descent to the substrate of the central zone of the cupola. The figure illustrates the growth of the jet and the generation of a counterjet. The $z(0, t)$ curve shows how a material particle, which was at the center of the heating spot prior to the USLP action, moves away

---

[10] These processes take place until the freezing of the cupola film begins. Heat removal and recrystallization processes should be analyzed separately.

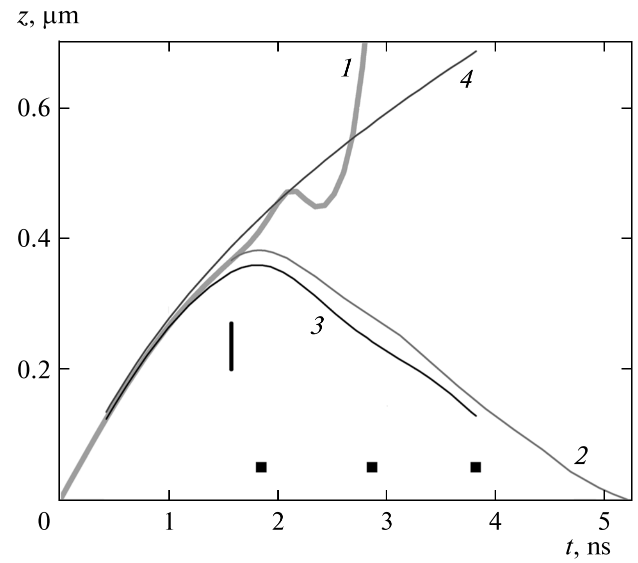

Fig. 20. Evolution of central zone including formation and evolution of intense axial formation. During nucleation, this formation has the form of a droplet at top (see Fig. 16). Then the droplet is transformed into jet and counterjet. The jet moves high above cupola surface with time. At instant $t = 3.8$ ns, the jet velocity is $\partial z_{\text{high}}/\partial t = 120$ m/s. It should be recalled that $v_0 = 300$ m/s (see parameters in Fig. 16). Curves *1*—$z(a = 0, t)$; *2*—$z_{\text{drop}}(t)$; *3*—$z_{\text{low}}(t)$; and *4*—$z_{\text{high}}(t)$. Dark squares correspond to instants pertaining to Figs. 16–19.

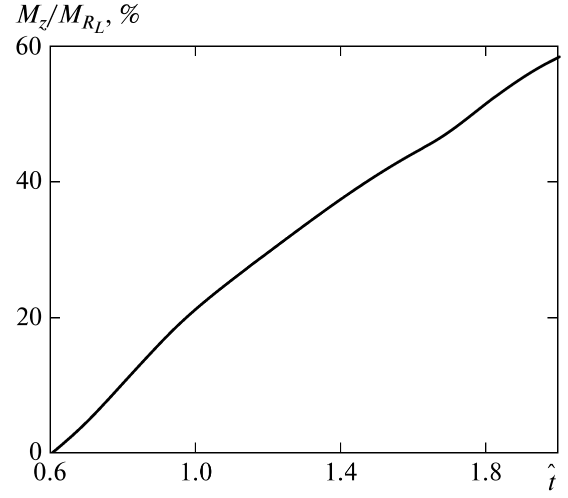

Fig. 21. Increase in mass fraction in percent. We are speaking of mass $M_z(t)$ which has passed by instant t through self-intersection point to axial zone in model (15). Quantity M_z is normalized to the mass M_{R_L} of film in the circle of radius R_L. At later instants, M_z is mainly mass of the jet emergent above cupola. In model (15), nucleation of axial formation occurs at the instant of self-intersection. This instant is marked by vertical segment in Fig. 20. Before the beginning of intersection, mass $M_z(t)$ is zero. Parameters are the same as in Fig. 16.

from the substrate in model (15). Soon after the self-intersection of the curve describing an infinitely thin film on the rz plane, trajectory $z(0, t)$ losses its physical meaning because film thickness cannot be disregarded in this zone. The curve $z_{\text{drop}}(t)$ in Fig. 20 corresponds to the trajectory of self-intersection point $a_{\text{drop}}(t)$, $r[a_{\text{drop}}(t), t] = 0$, and $z_{\text{drop}}(t) = z[a_{\text{drop}}(t), t]$. At this point, the thin film bulge in the form of a cupola intersects the z axis. Figure 16 clarifies the difference between points $z(0, t)$ and $z_{\text{drop}}(t)$—these points correspond to the upper and lower points of the loop. The instantaneous position of the film arc is specified by the solution $r(a, t)$, $z(a, t)$ to system (15). Here, parameter a runs through the arc. The point of interaction of arc $r(a, t)$, $z(a, t)$ with the z axis is shown in Figs. 16 and 17. In Fig. 20, the beginning of the curve $z_{\text{drop}}(t)$ is marked by a vertical segment. This point will be referred to as the instant of generation of the drop at the vertex of the cupola. The coordinates of the generation point are $t_{\text{drop}} = 1.571$ ns and $z_{\text{drop}} = 0.3663$ μm.

Let us compare the results of the MD simulation with the solution to system (15). In the MD computation, the drop is generated gradually. This corresponds to an increase in the distance between curves *3* and *4* in Fig. 20 along the z axis. The nucleation stage and subsequent evolution in the MD simulation are in conformity with the solution to system (15) (curves *1* and *2* in Fig. 20). As noted above, in the absence of film rupture, capillary forces always terminate the growth of the cupola. For the chosen parameters of the problem, the maximal separation of the cupola (0.37 μm) is attained at an instant of 1.8 ns at the return point of the motion to the substrate. Three squares in Fig. 20 mark the instants corresponding to Figs. 16–19.

Figure 21 shows how the amount of gold increases in the central zone. The final point of the graph is instant $t \approx 5.2$ ns, at which the self-intersection point in Fig. 20 arrives at the substrate. Dimensionless time $\hat{t}$ in Fig. 21 is laid along the abscissa axis. Dimensional time is $t = 2.60177\hat{t}$ ns. The substance that has passed from the film to the central zone is mainly spent on the formation of a powerful jet (Fig. 22). The diameter of the approximately cylindrical jet varies slowly, compared to its length. It amounts to approximately 50 nm (i.e., about 10% of the diameter of the circle in which the film spalls from the substrate).

Curve *3* in Fig. 17, which marks the outer boundary of the cupola, is removed. This is done to simplify Fig. 17. As a matter of fact, Fig. 17 illustrates the evolution of the cone-shaped cupola. The axial formation over its entire height is shown in Figs. 20 and 22. Let us consider the axial structure. In Fig. 22, the drop is located the upper part of the jet. The increase in the total length of formation, $z_{\text{high}}(x = 0, t) - z_{\text{low}}(x = 0, t)$, is shown in Fig. 20. At the initial stage ($t \approx 1.6$ ns) of the

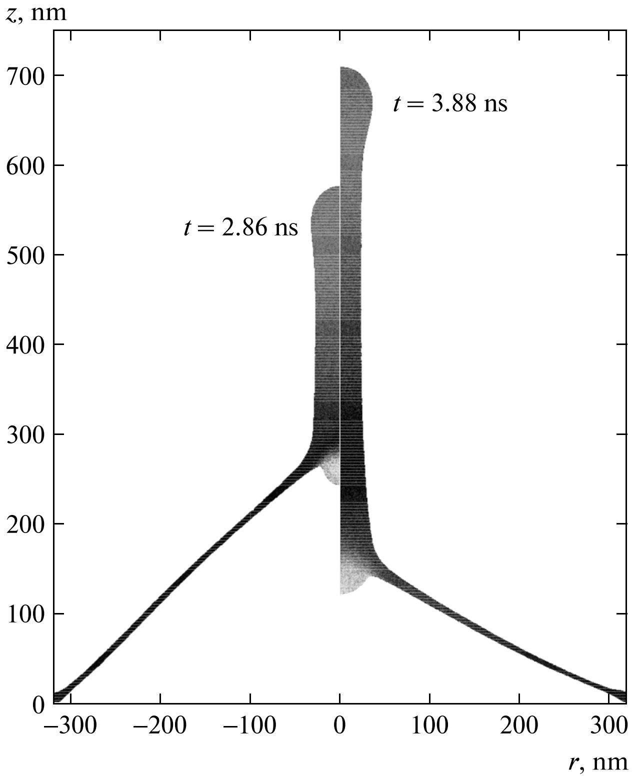

Fig. 22. Morphology and evolution of axial formation in axisymmetric case at late stages of MD simulations. Distributions of vertical velocity in a thin cross section passing through rotational axis of jet ($r = 0$) are shown. Right and left halves correspond to instants t = 3.88 and 2.86 ns, respectively. Upper point of jet on the right (left) moves up with a velocity of +131 m/s (+139 m/s), while lower point moves down with velocity of −164 m/s (−134 m/s).

flow of the substance to the z axis, the axial formation has the shape of a drop at the vertex of the cupola (see Figs. 16 and 20). At the next stage, the length of the jet increases much more rapidly than the length of the counterjet shown as a hump on the inner surface of the cupola in Figs. 17 and 22.

Cumulative effects are well known in engineering [82, 83]. Glancing collision of plane plates or the convergence of a cone to the axis of an incompressible liquid leads to the emergence of a cumulative jet (Fig. 23). An analogous situation takes place in our problem. The vertex of the counterjet has an appreciable velocity $v_{aj} = 120$ m/s directed downwards. Velocity $v_{\rm cup}$ of the substance in the cupola film close to the z axis is directed almost horizontally towards the axis; the vertical component of velocity of these particles is small. Since the film is located at an angle to the z axis, and velocity $v_{\rm cup}$ of the film is directed to the axis, the point of intersection of the generators of the cone-shaped cupola moves downwards. It turns out that the velocity of the point of intersection of the generators is approximately equal to the velocity of the tip of the counterjet. For this reason, in spite of considerable

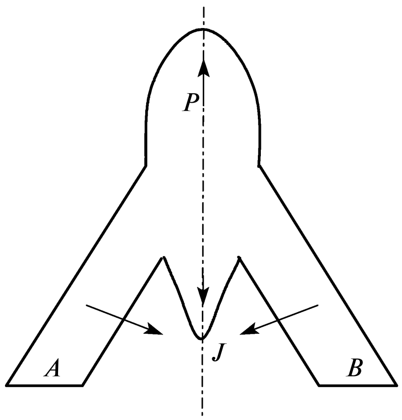

Fig. 23. Collision of plates A and B (planar geometry) or convergence of cone walls A and B to cone axis (axisymmetric case). Due to collision, cumulative jet J and pestle P appear. Arrows indicate directions of velocities of plates in laboratory system of coordinates.

velocity v_{aj} of the tip of the counterjet, the later develops slowly (cf. Fig. 7 in [28]). A longer counterjet is probably formed when the cupola begins freezing, and its velocity $v_{\rm cup}$ decreases. Nevertheless, it follows from Figs. 17 and 22 that an indication of the counterjet formation undoubtedly exists.

3.4. Classification of Solutions

The role of the classifier of solutions is played by the dimensionless velocity $\hat{V}_o$ (13). There are three types of solutions, corresponding to small, medium, and large values of this parameter: $\hat{V}_o \ll 1$, $\hat{V}_o \sim 1$, and $\hat{V}_o \gg 1$. Let us consider them in this order. For small values of velocity (13), the film separated from the substrate ascends to a small height $z \ll R_L$, $z \ll 1$, and then a turnover takes place, and the film returns to the substrate at instant $t_{\rm back}$ (see Fig. 24) with the departure and return of the axial point $z(a = 0, t)$ of the cupola to the plane $z = 0$ when $\hat{V}_o = 0.6$. For small amplitudes $\hat{V}_o$, the film stretched on the circle of radius R_L could perform capillary oscillations if the substrate were not present. Instant $t_{\rm back}$ of the impact of the film against the substrate is equal to approximately half the period of oscillations at the lower mode. Figure 24 shows dependences $z(0, t; \hat{V}_o)$ at various values of velocity $\hat{V}_o$ (13). Even for small values of $\hat{V}_o \ll 1$, the $z(t)$ curve differs from a sinusoid, because function (18) specifying the initial distribution of velocity $z(a, t = -0)$ is proportional to the square of the cosine and is not an eigenmode of the problem of film oscillations on the circular contour. The maximal height of the film above the substrate is attained at instant $t_{\rm max} \approx t_{\rm back}/2$, approx-

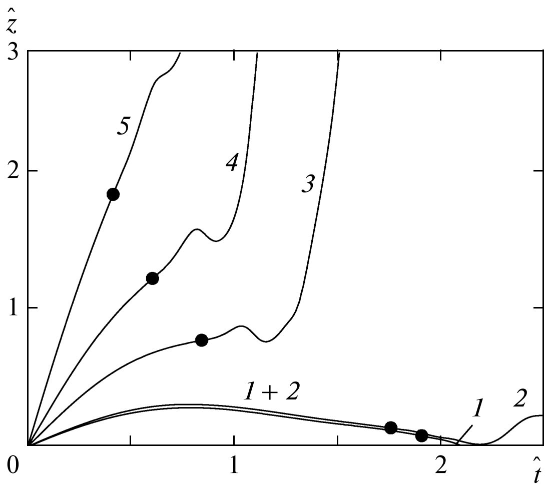

Fig. 24. Modification of solutions upon variation of the ratio of the kinetic and capillary energies (see Eqs. (12) and (13)). Time dependences $z(0, t; \hat{V}_o)$ are shown for (*1*) $\hat{V}_o$ = 0.6, (*2*) 0.65, (*3*) 1.5, (*4*) 2.6, and (*5*) 5. The larger the parameter $\hat{V}_o$, the higher the kinetic energy and the film velocity. The case where $\hat{V}_o = 2.60177$ is analyzed in detail above (see Figs. 20 and 16–22). Markers indicate points of formation of the drop ($\hat{t}_{\rm drop}$, $\hat{z}_{\rm drop}$) and the apex.

imately equal to a quarter of the period. In dimensionless coordinates $t/(R_L/v_\sigma)$, we have $\hat{t}_{\max} \approx 1$.

The limitation $z \ll 1$ corresponds to the linear theory of perturbation amplitude. Let us carry out the linear analysis. This will allow us to calculate the above-mentioned instants $\hat{t}_{\max}$ of attainment of the maximum height and $t_{\rm back}$ of impact of the film against the substrate at the limit of small amplitudes $\hat{V}_o \ll 1$. It will be shown that these instants attain constant values at the limit $\hat{V}_o \longrightarrow 0$. In addition, the linear solution has the following merits. The film begins moving from the plane $z = 0$, when the condition $z \ll 1$ is observed. Therefore, the linear solution describes the initial stage of the evolution for arbitrary values of $\hat{V}_o$ (13). The duration of this stage is bounded by a value equal to a small fraction of time $1/\hat{V}_o$ (in dimensional variables, this time is equal to R_L/v_o).

Let us calculate the period of small capillary oscillations of a film stretched on a circle of radius R_L. Linearizing system (15) in the vicinity of the unperturbed state ($\hat{r} = \hat{a} + \delta r$, $|\delta r| \ll 1$, $|z| \ll 1$), we obtain

$$k \equiv \frac{ds}{da} = 1, \quad \hat{R} = \frac{1}{\partial^2\hat{z}/\partial\hat{a}^2}, \quad C = \frac{1}{2}\left(\hat{z}'' + \frac{\hat{z}'}{\hat{a}}\right),$$

where $\hat{z}' = \partial\hat{z}/\partial\hat{a}$. Dimensionless variables were introduced above (see relations (14)). Substituting these relations into system (15), we find that correction δr is a second-order correction, which is zero in the linear approximation. It can be seen that to a first approximation, the material particles of the film perform oscillations, moving strictly along the normal (in the linear approximation). The equation for $\partial^2 r/\partial t^2$ falls out of system (15); function $r(a, t)$ and Lagrangian coordinate a can be replaced by the horizontal coordinate (radius r of the cylinder). The linearized equation for $\partial^2 z/\partial t^2$ has the form

$$\hat{z}'' + \frac{\hat{z}'}{\hat{r}} - 2\frac{\partial^2\hat{z}}{\partial\hat{t}^2} = 0, \quad \hat{z}' = \frac{\partial\hat{z}}{\partial\hat{r}}. \tag{22}$$

We seek its solution in the form $\hat{z}(\hat{r}, \hat{t}) = \exp(-i\hat{\omega}\hat{t})Z(\hat{r})$. Substituting this into Eq. (22), we find that function Z satisfies the zeroth-order Bessel equation

$$\hat{r}Z' + Z' + 2\hat{\omega}^2\hat{r}Z = 0. \tag{23}$$

The solution to Eq. (23) we are interested in has the form $Z \propto J_0(\sqrt{2}\hat{\omega}\hat{r})$. The second independent solution can be omitted because it has a logarithmic singularity in the axis $r = 0$. Using boundary condition (20) for $\hat{r} = 1$ ($\hat{r} = r/R_L$ (14)), we can determine the eigenmode spectrum

$$\hat{\omega}_i = \frac{b_i}{\sqrt{2}}, \quad \hat{T}_i = \frac{2\pi}{\hat{\omega}_i}, \quad T_i = \frac{2\sqrt{2}\pi}{b_i}\frac{R_L}{v_\sigma}, \tag{24}$$

where b_i are the roots of the equation $J_0(b_i) = 0$. The first three values are $b_1 = 2.4048255$, $b_2 = 5.5200781$, and $b_3 = 8.6537279$. The period of the fundamental mode is $\hat{T}_1 = 3.69497$.

Let us expand dimensionless initial velocity (18) into a series in the Bessel functions:

$$\hat{V}_o\cos^2\left(\frac{\pi\hat{r}}{2}\right) = \hat{V}_o\sum_{i=1}^{\infty} a_i J_0(b_i\hat{r}), \tag{25}$$

where the expansion coefficients are given by

$$a_i = \frac{\int\cos^2\left(\frac{\pi\hat{r}}{2}\right)J_0(b_i\hat{r})rdr}{\int J_0^2(b_i\hat{r})rdr}.$$

For several first values of coefficients (25), we obtain $a_1 = 0.7793$, $a_2 = 0.26771$, and $a_3 = -0.06562$. The solution of the problem of the motion of the cupola apex of the film is given by the converging series

$$\hat{z}(\hat{r}, \hat{t}) = \hat{V}_o\sum_{i=1}^{\infty}\frac{a_i}{\hat{\omega}_i}\sin(\hat{\omega}_i\hat{t})J_0(b_0\hat{r}).$$

Using this series, we can determine instants $t_{\rm back}$, $\hat{t}_{\max}$, and the maximal distance between the film and the substrate, $\hat{z}(\hat{r} = 0, \hat{t}_{\max})$, in the limit $\hat{V}_o \longrightarrow 0$. The values of $t_{\max}$ and $t_{\rm back}$ define the point of the maximal ascent of the film and the instant of the impact of the film against the substrate (see Fig. 24, curve $z(0, t; \hat{V}_o = 0.6)$). These instants are the roots of the equations

$$\hat{z}(\hat{r} = 0, \hat{t}_{\rm back}) = 0, \quad \hat{t}_{\rm back} = 1.94128,$$
$$\frac{\partial \hat{z}(\hat{r} = 0, \hat{t}_{\max})}{\partial \hat{t}} = 0, \quad \hat{t}_{\max} = 0.736047. \qquad (26)$$
$$\hat{z}(\hat{r} = 0, \hat{t}_{\max} = 0.736047) = 0.463843\hat{V}_o.$$

Initial velocity $\partial\hat{z}(\hat{a}, \hat{t} = 0)/\partial\hat{t} = \hat{V}_o\cos^2(\pi\hat{a}/2)$ (18) is a mixture of modes. For this reason, time $\hat{t}_{\max} = 0.736$ is not equal to half the time of return to the substrate ($\hat{t}_{\rm back}/2 = 0.97$), and the return time $\hat{t}_{\rm back} = 1.94$ is not equal to half the period of the lowest mode ($\hat{T}_1/2 = 1.85$).

The linear solution is compared with the solution to complete system (15) in Fig. 25. A noticeable deviation from the linear solution begins after the formation of the droplet. The droplet is formed at points ($t_{\rm drop}$, $z_{\rm drop}$) indicated by markers in Fig. 25. At $t > t_{\rm drop}$, the mass of the axial formation begins to increase from zero (see Fig. 21). In addition, in the solution to system (15), two points instead of one appear on the z axis (see the loop in the top part of Fig. 16 and Fig. 20). Namely, apart from point $z(a = 0, t)$, self-intersection point $z_{\rm drop}(t)$ appears. Figure 22 shows an intense axial structure into which the initially small droplet is gradually transformed.

For small values of $\hat{V}_o$, the amplitude is $|z| \sim \hat{V}_o$; in this case, the droplet is formed at the late stage. As a matter of fact, the time of formation of the droplet on the surface with a small curvature is long. Time $t_{\rm drop}$ rapidly increases with decreasing value of $\hat{V}_o$ (see Figs. 24–26). An increase in velocity $\hat{V}_o$ (13) in the nonlinear system leads to a slight increase in the value of $\hat{t}_{\max}$. For $\hat{V}_o < 1.4$, the time $\hat{t}_{\rm drop}(\hat{V}_o)$ of drop formation is longer than $\hat{t}_{\max}$. This means that the droplet is formed on the descending branch of the time dependence $z(0, t; \hat{V}_o)$. For $\hat{V}_o < 0.555$, we have $\hat{t}_{\rm drop}(\hat{V}_o) > \hat{t}_{\rm back}(\hat{V}_o)$; i.e., for small amplitudes, the drop has no time to be formed on the entire time interval $(0, t_{\rm back})$ of existence of the film in its flight from the instant of its separation from the substrate to the instant of its return to the substrate. Accordingly, time dependence $z(0, t; \hat{V}_o)$ for $\hat{V}_o < 0.555$ has no point of drop formation. For $\hat{V}_o > 0.555$, the drop generation point on the $z(0, t; \hat{V}_o)$ curve exists (see Figs. 24 and 25). At point $\hat{V}_o = 0.555$, $\hat{t} = 2.09$, the curves $\hat{t}_{\rm back}(\hat{V}_o)$ and $\hat{t}_{\rm drop}(\hat{V}_o)$ intersect (Fig. 26).

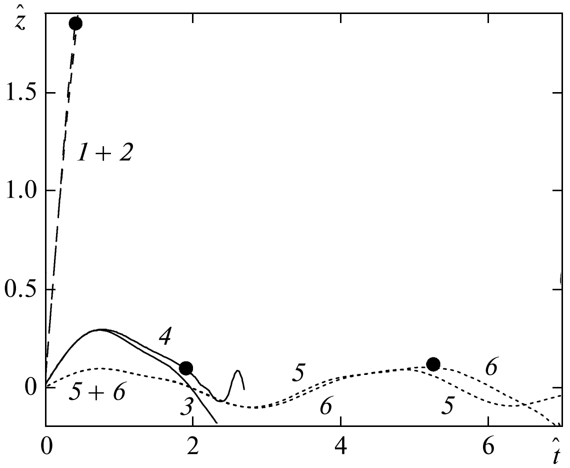

Fig. 25. Comparison of linear (curves *1*, *3*, *5*) and nonlinear (curves *2*, *4*, *6*) solutions to system (15) for $\hat{V}_o$ = (*1*, *2*) 5, (*3*, *4*) 0.6, and (*5*, *6*) 0.2. The formation of the drop at the apex indicates that nonlinear corrections have become significant. As in Fig. 24, bullets ($\hat{t}_{\rm drop}$, $\hat{z}_{\rm drop}$) correspond to the instant of emergence of the drop and to the position in which it is located.

For $\hat{V}_o > 0.555$, the drop has time to be generated during the flight of the cupola. After its formation ($t > t_{\rm drop}$), the $z(0, t; \hat{V}_o)$ dependence becomes rather conditional. Indeed (see Fig. 20), three points appear on the z axis (from bottom to top): the apex of the counterjet (curve *3*); joining of the cupola with the central zone (curve *2*); and apex of the jet (curve *4*) (see also Fig. 22). Functions $\hat{t}_{\rm drop}(\hat{V}_o)$ and $\hat{z}_{\rm drop}(\hat{V}_o)$ give the coordinates of the point of drop nucleation at the cupola apex, which are shown by markers in Figs. 24 and 25. It can be seen from Fig. 24 that the distance $\hat{z}_{\rm drop}(\hat{V}_o)$ over which the droplet is formed increases with parameter $\hat{V}_o$. However, the time $\hat{t}_{\rm drop}(\hat{V}_o)$ of drop formation decreases thereby. These two circumstances are associated with the increase in velocity $\hat{V}_o$.

It follows from the above arguments that the asymptotic form for $\hat{V}_o \ll 1$ is quite simple. Let us consider the opposite limit $\hat{V}_o \gg 1$ (see Figs. 24–26). Surface tension stops the cupola for an arbitrary high kinetic energy. However, the z coordinate of the stop point will be large in this case. If the cupola is stopped, the droplet will surely be formed. Naturally, these arguments are only valid for an infinite tensility of film. In fact, under the USLP conditions for thin films (d_f = 10–100 nm), the film ruptures under extension down to a thickness of 1 nm. It follows from analysis of the dependence of the instantaneous film thickness on the radius (see Fig. 19) that the rupture occurs approximately over the circle close to the base of the cupola

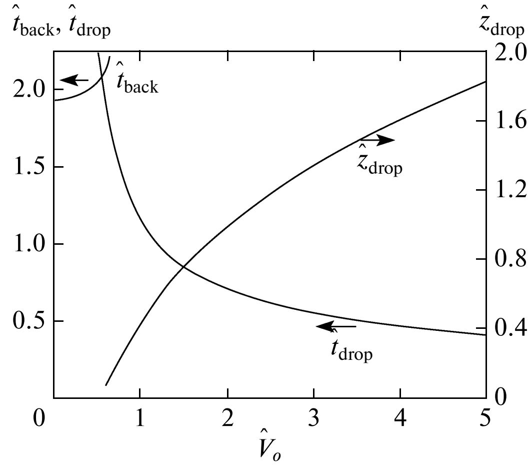

Fig. 26. Classification of solutions depending on parameter $\hat V_o$ (13). For $\hat V_o > 0.6435$, film does not return to substrate. Point $\hat V_o = 0.6435$, $\hat t_{\rm back} = 2.22$ is point of termination of $\hat t_{\rm back}(\hat V_o)$ curve. Curves $z(0, t; \hat V_o)$ in Fig. 24 for $\hat V_o = 0.6$ and 0.65 border critical value $\hat V_o = 0.6435$. Functions $\hat t_{\rm drop}(\hat V_o)$ and $\hat z_{\rm drop}(\hat V_o)$ specify coordinates of point of drop nucleation at apex of cupola. These functions parametrically define the curve, individual points of which are indicated by markers in Figs. 24 and 25.

(if we disregard crystallization). In this case, a circular hole appears in the film covering the substrate.

If we specify initial distribution (18) and assume that surface tension $\sigma = 0$, $v_\sigma = 0$, and $\hat V_o = \infty$, the right-hand side of system (15) vanishes; i.e., the substance of the film flies by inertia with a constant velocity along the normal to the substrate surface:

$$\hat r(\hat a, \hat t) = \hat a, \quad \hat z(\hat a, \hat t) = \hat V_o \hat t \cos^2(\pi \hat a/2). \tag{27}$$

For large radii R_L of the heating spot, analysis is confined to this assumption, but in the case of foaming, capillary effects should be taken into account [55, 76–78]. The motion described by Eqs. (27) stretches the film. Let us calculate the extent of stretching using formula (21):

$$\frac{h}{h_o} = \frac{a/r}{s'_a} = \frac{1}{s'_a} = \frac{1}{\sqrt{1+\left[\frac{\pi}{2}\hat V_o \hat t \sin(\pi \hat a)\right]^2}}.$$

In product $\hat V_o \hat t$, the capillary velocity v_σ is cancelled out. It can be seen that the maximum extension corresponds to the point of inflection of the initial velocity profile (i.e., at the middle of segment $(0, R_L)$). At the ends of this segment, extension is absent ($h = h_o$), while at the middle of the segment, the film thickness decreases in accordance with the law

$$\frac{h}{h_o} = \frac{1}{1+\frac{\pi^2}{4}\left(\frac{v_o t}{R_L}\right)^2}$$

with the asymptotic form

$$\frac{2}{\pi}\frac{R_L}{v_o t} = \frac{2}{\pi}\frac{R_L}{z(a=0, t)}$$

over long time intervals.

3.5. Blistering in Planar Geometry

The axisymmetric case $2D_a$ (15), (16) is qualitatively similar to the planar case $2D_p$ (17). Therefore, we can use the scheme employed above, viz., the linear solution, the classification in parameter $\hat V_o$, and comparison of the linear, nonlinear, and MD solutions. The linearization of $2D_p$ system (17) leads to the wave equation

$$z_{tt} - v_\sigma^2 z''/2 = 0, \tag{28}$$

or

$$\hat z_{tt} - \hat z''/2 = 0.$$

In addition, in the linear approximation, we can disregard the displacement of Lagrangian particles in the horizontal direction x; in $2D_p$ geometry, coordinate x is used instead of radius r. Accordingly, $x(a, t) = a$, $a \longrightarrow x$. Substituting $\hat z(\hat x, t) = \exp(-i\hat\omega\hat t)Z(\hat x)$, we obtain

$$Z'' + 2\hat\omega^2 Z = 0.$$

This equation replaces Eq. (23) for cylindrical waves.

We are interested in standing capillary waves. In the general case, such a wave is the superposition of eigenmodes

$$\hat z(\hat x, \hat t) = \hat V_o \sum_{m=1}^{\infty} \frac{a_m}{\hat\omega_m} \sin(\hat\omega_m, \hat t) \cos\frac{\pi(2m-1)\hat x}{2} \tag{29}$$

with the discrete spectrum

$$\hat\omega_m = \frac{\pi(2m-1)}{2\sqrt{2}},$$

$$\hat T_m = \frac{2\pi}{\hat\omega_m} = \frac{4\sqrt{2}}{2m-1}, \quad m = 1, 2, \ldots$$

The period of the first mode is $\hat T_1 = 4\sqrt{2} = 5.657$. It can be seen that due to the decrease in the total curvature of the film (in the $2D_p$ case, curvature $1/R_t$ is zero; see Eqs. (16), (17)), this period is considerably larger than the period $\hat T_1^{2Da} = 3.695$ (24) of the first mode of a cylindrical standing wave.

Coefficients a_m of Fourier series (29) are determined by the initial velocity profile (18):

$$a_m = \frac{\int_{-1}^{1}\cos^2(\pi\hat{x}/2)\cos[\pi(2m-1)\hat{x}/2]d\hat{x}}{\int_{-1}^{1}\cos^2[\pi(2m-1)\hat{x}/2]d\hat{x}} \tag{30}$$
$$= -\frac{(8/\pi)\cos(\pi m)}{(-3-4m+4m^2)(1-2m)}.$$

Fourier expansion (29) with coefficients (30) completely determines the linear solution. It should be noted that binomial $\cos^2(\pi\hat{x}/2) = 1/2 + (1/2)\cos(\pi\hat{x})$ is not a segment of series (29). Indeed, neither the constant nor $\cos(\pi\hat{x})$ satisfy boundary conditions (20) separately; consequently, these quantities are not the eigenmodes of the problem.

Linear solution (29), (30) makes it possible to determine coordinates $t_{\max}$, $z_{\max}$ of the stop point for the cupola in its upward motion and instant t_{back} of the impact of the film against the substrate (see Eq. (26)). These values correspond to the limit of small parameters $\hat{V}_o$ (13). In $2D_p$ geometry, we obtain

$$\hat{t}_{\text{back}} = 2.82843(1.94128),$$
$$\hat{t}_{\max} = 1.41421(0.736047),$$
$$\hat{z}_{\max} = \hat{z}(\hat{x} = 0, \hat{t}_{\max} = 1.41421)$$
$$= 0.707155\hat{V}_o(0.463843\hat{V}_o).$$

Here, the values of expression (26) corresponding to $2D_a$ geometry are given in parentheses for comparison. It can be seen that a decrease in the curvature in $2D_p$ geometry is manifested in an increase in times $t_{\max}$ and t_{back} and in an increase in coordinate $z_{\max}$ of the stop point.

The classification of solutions depending on dimensionless velocity $\hat{V}_o$ (13) is illustrated in Fig. 27, which is a generalization of Figs. 24 and 25 to the case of $2D_p$ geometry. The curves in the figure correspond to three MD calculations in $2D_p$ geometry for the following values of parameter $\hat{V}_o$: 0.776379, 1.21293, and 2.56695 (their rounded values are given in Fig. 27). The higher the velocity, the longer the distance to which the apex of the cupola ascends above the substrate plane $z = 0$. Smoother curves correspond to linear solution (29), (30) and lie lower. Nonlinear effects become important when the nonlinear solution substantially deviates from the linear solution.

In Figs. 28–30, the results of the MD simulation and the numerical solution based on system (17) are compared. The results correspond to late instants at which the substance of the film is noticeably concentrated in the central zone. For this reason, description (17) in the axial region becomes inapplicable in the infinitely thin film approximation. Nevertheless, outside this region, the solution to system (17) is in good agreement with the results of the MD calculations. Satisfactory agreement is preserved over long time intervals even in the case of a thick film (see Fig. 28). In the MD calculation illustrated in this figure, the mass per unit film area after thermalization by the thermostat and immediately before the beginning of motion is $\mu_o = 5.27 \times 10^{-5}$ g/cm^2. The corresponding thickness is $h_o = 32$ nm and $R_L/h_o = 6.9$.

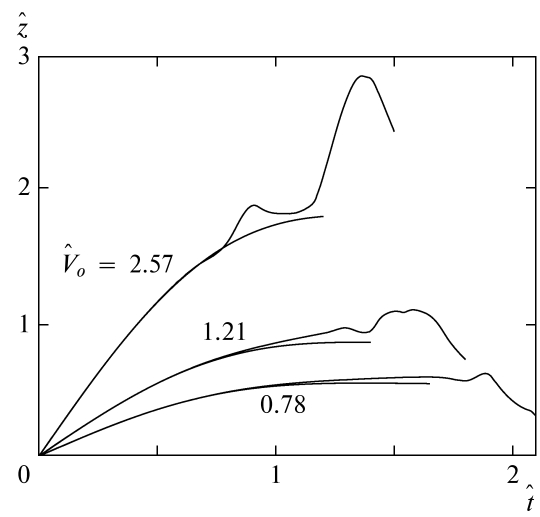

Fig. 27. Ascent of the apex of the cupola in the $2D_p$ geometry. Trajectories $z(a = 0, t)$ of apex are plotted in accordance with solution to nonlinear system (17) (upper curves) in comparison with linear solution (29) (lower curves). In each pair, complete solution lies above and is more intricate.

We chose various parameters for MD calculations to estimate the effect of physical conditions on blistering. In our calculations (see Fig. 28), the dimensionless velocity was $\hat{V}_o = 0.776379$. The remaining parameters were as follows: initial velocity v_o = 50 m/s, number of atoms $N_{\text{at}} = 2976320 \approx 3 \times 10^6$, $R_L = 220$ nm, thickness of the computational domain along the coordinate perpendicular to the plane of Fig. 28 $l_\perp = 4.2$ nm, and $v_\sigma = 64.4$ m/s; in all computations, gold was heated to 1600 K, the surface tension at this temperature was 546 dyne/cm, and the equilibrium density was 16.55 g/cm^3 (see Appendix).

The parameters of the MD computations depicted in Fig. 29 are as follows: $\hat{V}_o = 1.21293$; $v_o = 150$ m/s; $R_L = 310$ nm; $N_{\text{at}} = 1093752 \approx 1.1 \times 10^6$; $l_\perp = 4.04$ nm; $\mu_o = 1.43 \times 10^{-5}$ g/cm^2; $h_o = 8.63$ nm; and v_σ = 124 m/s.

The MD computation depicted in Fig. 30 had the following parameters: $\hat{V}_o = 2.56695$; $v_o = 300$ m/s; $R_L = 310$ nm; $N_{\text{at}} = 1169640 \approx 1.2 \times 10^6$; $l_\perp$ =

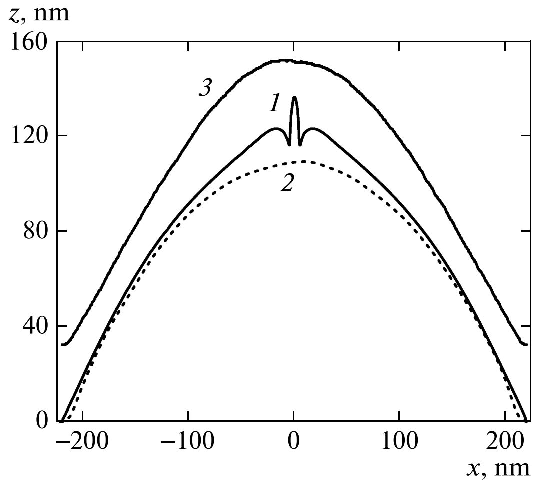

Fig. 28. Comparison of results of MD computation (curves *2* and *3*) and model (17) (curve *1*); see Fig. 16. Parameters of MD computations: thick film of initial thickness $h = 32$ nm, $\hat{V}_o = 0.776379$. Dimensionless time $\hat{t} = 1.89$ ($t = 6.47$ ns) is used so that this figure can be compared with Fig. 27.

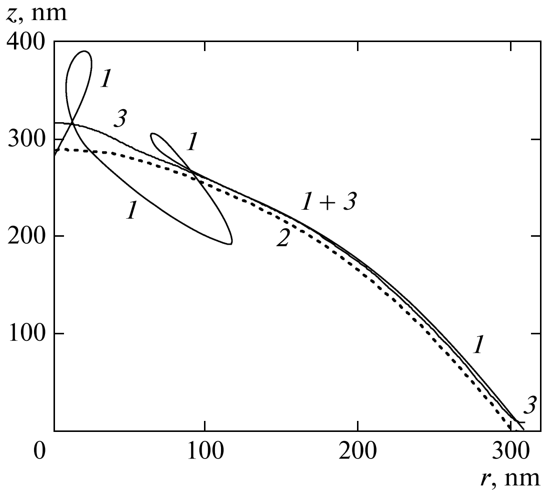

Fig. 29. Comparison of results of MD simulation (curves *2*, and *3*) and model (17) (curve *1*) for a film with a thickness of 1/3 of the thickness in Fig. 28, thrice as high velocity, and size R_L increased by a factor of 1.5 (see also caption to Fig. 16). $\hat{V}_o = 1.21293$, $\hat{t} = 1.75$ ($t = 4.39$ ns).

3.865 nm; $\mu_o = 1.60 \times 10^{-5}$ g/cm²; $h_o = 9.7$ nm; and $v_\sigma = 117$ m/s.

Pay attention to a slight instability in the MD computations in Fig. 28. It violates the symmetry $x \longrightarrow -x$. This phenomenon is associated with thermal fluctuations (initiation, no exact symmetry) and deceleration (enhancement of perturbations). The instability leads to symmetry breaking during the decay of the liquid film into drops (see below). In calculations based on model (17) at elevated values of the initial dimensionless velocity, the instability is manifested more strongly (cf. Figs. 28, 29, and 30). It embraces the central zone of the cupola. In the $2D_a$ geometry, the accumulation of nonlinear effects is manifested primarily in the formation of a drop on the z axis (see Figs. 16, 24, and 25). Outside the drop, the surface of the cupola remains smooth for some time. In the $2D_p$ geometry, the "stirring" of the axial zone can begin prior to the formation of the central drop (see Figs. 28 and 29). In model (17), we assume that the formation of the drop begins after the self-intersection of the film. Outside the central zone of the cupola, the solution in model (17) and the results of the MD simulation are in good agreement (see Figs. 29 and 30). In the $2D_p$ geometry, the maximal extension of the film and, accordingly, its minimal thickness are closer to the central zone than in the $2D_a$ geometry (see Figs. 29 and 30).

3.6. Rupture of the Film

The rupture of the cupola because of its stretching and a decrease in thickness to about 1 nm is illustrated in Fig. 31 (see also Fig. 3c from [84]). The rupture occurs instantaneously at $t \approx 4.44$ ns; apparently, this process is associated with the development of a viable nucleus due to thermal fluctuation on the strongly stretched film. The duration of the process is about 10 ps (see Fig. 31). The effects associated with the beginning of puncture and its 3D evolution were considered in [84]. The parameters of the MD computation presented in Figs. 30 and 31 are identical. The vertical and horizontal digitization step (pixel size) for the MD data was 0.8 nm.

The dispersion relation for capillary waves on deep water has the form $\omega = \sqrt{\sigma/\rho}\, k^{3/2}$, where ρ is the density of water. Small-amplitude oscillations on a thin film are described by wave equation (28). The substitution of $z \propto \exp(-i\omega t + ikx)$ into Eq. (28) determines the linear dispersion relation in wave vector k:

$$\omega = (v_\sigma/\sqrt{2})k. \tag{31}$$

According to this equation, the phase and group velocities of the surface wave are identical and are $v_\sigma/\sqrt{2}$. Thus, the wave associated with surface tension on a thin film is analogous to an acoustic wave in an elastic medium.

Film rupture (see example in Fig. 31) causes a sharp change in force-induced stresses. In accordance with Eqs. (28) and (31), the signal from the rupture propagates over the film with a finite velocity $v_\sigma/\sqrt{2}$. The dynamics of formation and expansion of the rupture has some features in common with the dynamics of nucleation of a void [85] in a stretched condensed material. In the case of a bulk medium, the perturbation from the rupture is localized in the region between the spall pulse and the boundary of the vapor-filled cavity. This pulse propagates from the point of rupture

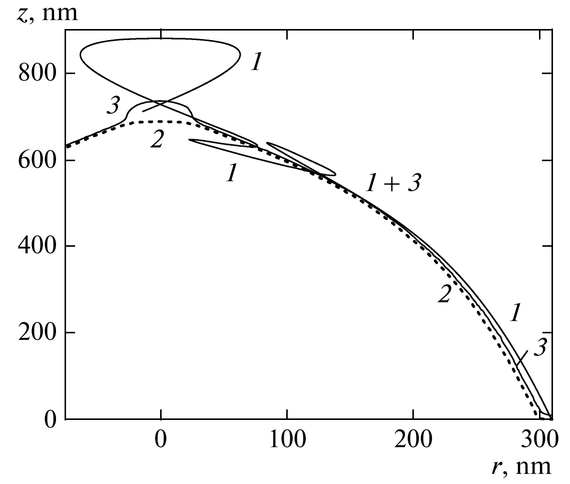

Fig. 30. Comparison of results of MD computation and model (17) for high initial velocity $v_0 = 300$ m/s (twice as high as in Fig. 29); notation of curves is same as in Figs. 16, 28, and 29, $\hat{V}_0 = 2.56695$, $\hat{t} = 1.4$ ($t = 3.71$ ns).

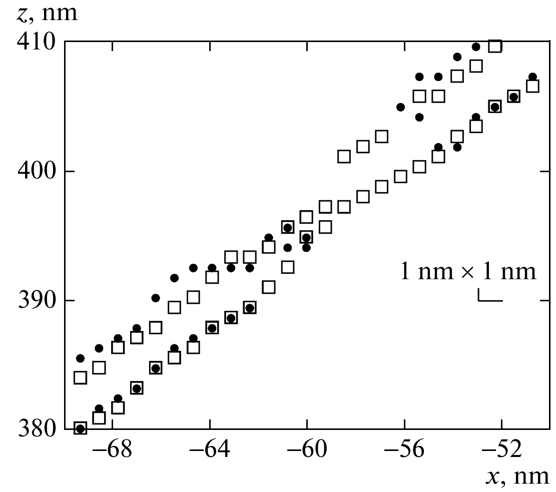

Fig. 31. Rupture of film due to its extension. Parameters are same as in Fig. 30. Markers trace film boundary. Two instants are represented: immediately before rupture, $t = 4.435$ ns (squares) and immediately after it (circles), $t = 4.454$ ns.

with the velocity of sound. The spall pulse removes the stress (unloads the stretched material) because behind it the stretched (negative pressure $p < 0$) substance is compressed to the normal state ($p \longrightarrow 0$). Thus, a spall pulse is a compression wave that elevates pressure from $p < 0$ to $p \approx 0$. Due to a decrease in the specific volume upon the removal of stress (unloading), the volume of the cavity (discontinuity) emerging during nucleation increases. At the initial stage of nucleation, the velocity of the spall pulse and of the expansion rate of the cavity are comparable. Then the expansion of the cavity is sharply decelerated and passes to a strongly subsonic regime of motion.

Ordinary sound propagates in the gold melt heated to 1600 K with a velocity approximately equal to 2.25 km/s [36, 37, 53, 54]. The traces of its propagation cannot be seen on the film. As a matter of fact, the film is thin and is in contact on both sides with the region of constant pressure (vacuum). For this reason, ordinary sound propagating over the film dies away over a distance of the order of the film thickness. Let us analyze the situation with sound described by Eqs. (28), (31).

Figure 32 shows the instantaneous distribution of the horizontal velocity component $v_x(x, t = 4.512$ ns) in the vicinity of rupture shown in Fig. 31 at 70 ns after the rupture. The rupture is singled out by two vertical lines (the "gap" in Figs. 32 and 33), which correspond to the same instant. The ellipse at the bottom marks a tiny independent drop separated during rupture. Another droplet is formed at the right bank of the rupture (see Fig. 33). It is also shown by an ellipse. The size of these droplets is smaller than a nanometer. Two velocity jumps propagate from the rupture in the film to both sides (see Fig. 32). The jump propagating to the left is marked by the vertical arrow in Fig. 32. The left vertical in Fig. 33 is located at the same point. The right jump propagates towards the central drop. At instant $t = 4.512$ ns shown in Figs. 32 and 33, the coordinate of the right jump is $x = -40$ nm. The horizontal size of the left half of the central drop is marked by the two-sided horizontal arrow in Fig. 32. Within the central drop, the horizontal velocity component v_x is close to zero. This is due to the fact that the mass flows entering the central drop from the left and right impart horizontal momenta of opposite signs to the drop.

The calculation of the velocity of the substance behind the jump relative to the substance of the film before the jump gives $\Delta v_t = 165$ m/s at instant $t = 4.512$ ns corresponding to Figs. 32 and 33. To calculate the value of Δv_t, velocity vectors $\mathbf{v}_-$ on the left and $\mathbf{v}_+$ on the right of the jump were subtracted. The projection of difference $\mathbf{v}_- - \mathbf{v}_+$ on the direction along the film is Δv_t. Calculation of velocity $v_\sigma/\sqrt{2}$ (31) by formula (12), taking into account the decrease in the film thickness to 2.35 nm, gives 168 m/s. It follows that at the initial stage after the rupture, the front of the jump propagates over the film at the velocity of sound (31). In this sense, this front resembles the spall pulse that also propagates with the velocity of sound (low-intensity shock wave).

Figure 34 illustrates the situation at instant $t = 4.896$ ns, when there are three ruptures on the surface of the cupola. The instants of formation of ruptures are indicated in each case. The further evolution of the cupola in Fig. 34 includes the formation of the central drop that absorbs a piece of film from the third rupture (4.87 ns) and the formation of the left-side drop. Both drops move upwards. The left side drop absorbs a piece

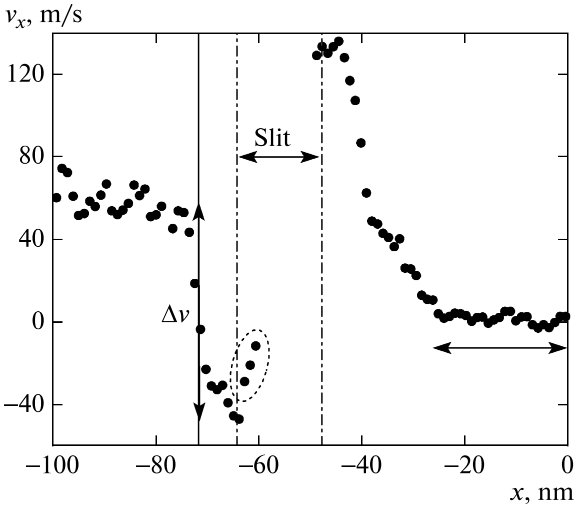

Fig. 32. Velocity jump resembling spall pulse at instant $t = 4.512$ ns. Jump front is shown by vertical arrow Δv. This front is on left from rupture (slit). Front propagating to the right is located at this instant at point $x = -40$ nm. Parameters of computation correspond to the high-velocity case depicted in Fig. 30. Two-sided horizontal arrow marks position of central drop formed at cupola apex (see Figs. 30 and 33).

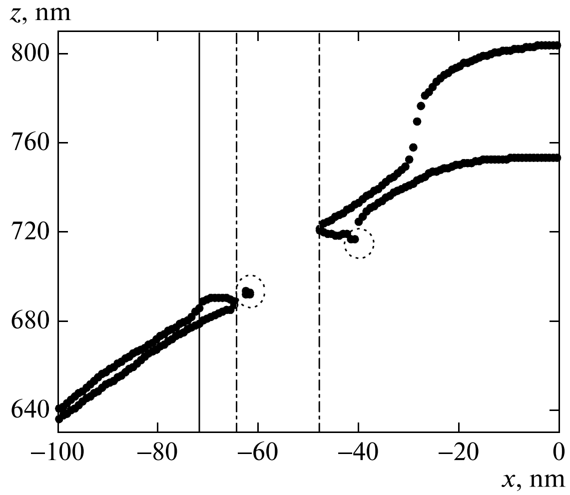

Fig. 33. Formation of drops (bulges) at rupture banks. These are new drops relative to central drop. Tiny nanodrops shown by circles are insignificant. It can be seen that the velocity jump front in Fig. 32 coincides with boundary between the drop and film. Jump is shown by vertical arrow in Fig. 32 and by continuous straight line in this figure.

of the film between the first (4.44 ns) and second (4.76 ns) ruptures. The second rupture occurs independently from the first one. Although the first rupture (like the spall pulse) terminates the stretching of the film, the region of increasing film thickness (in which the spall pulse is acting and stops stretching) is bounded to the drop. For this reason, the stretching of the film outside the drop continues, and the second rupture takes place.

Figure 35 shows the shape of the drop from Fig. 33, but at a later instant. Like Fig. 32, Fig. 35 also shows the velocity distribution. The computation of the velocity of the drop relative to the film substance and the comparison of this velocity with the local running velocity of sound (31) show that the velocity jump continues its propagation at the velocity of sound! This is astonishing. Indeed, the drop is large, and the time elapsed since its formation is 456 ps, but it still moves with the velocity of sound as a small perturbation of the system of equations (17) (cf. Fig. 32). It turns out that the velocity jump is equivalent to the spall pulse in the bulk case, the drop is equivalent to the region of compression between the spall pulse front and the cavity, and the 3D cavity is equivalent to the film rupture. This contradicts the obviously nonlinear form of the flow in the presence of a coarse drop. A film ⟶ film transformation upon a transition through the velocity jump is not seen. Instead of this, the substance of the film is absorbed by the drop. The latter cannot be treated as a film. It may appear that the drop must act as a sort of the boundary condition imposed on the film outside the drop (in this connection, see Figs. 16, 29, and 30 with the central drop and adjoining film; see also the discussion where these figures are compared with the results of MD simulation).

The coincidence of the velocity of the drop (relative to the substance of the film in front of it) with the velocity of sound (31) can be explained as follows. Let us write the law of conservation of momentum

$$2\sigma t = d_f l \rho \Delta v. \qquad (32)$$

The left-hand side of the momentum balance equation (32) contains the force acting on the drop, and the right-hand side is the gained momentum. Coefficient 2 appears because the film has two surfaces. This momentum is accumulated over time t. During this time, a piece of the film of length l is absorbed by the drop. The film thickness is denoted by d_f. Upon the intersection of the velocity-jump front (which is simultaneously the boundary of the drop), the velocity of a particle of the substance changes by Δv. The material particle in the drop and the velocity jump front move with velocity Δv relative to the film substance. Substituting the kinematic condition $l = t\Delta v$ into Eq. (32), we obtain

$$\Delta v = v_\sigma/\sqrt{2}, \qquad (33)$$

i.e., the law of conservation of momentum makes the drop move at the velocity of sound (31).

Let us write the law of conservation of energy. Let the film be at rest. A drop approaches the film from one of its ends. For example, the drop in Fig. 35 moves from right to left. The velocity of the drop relative to the film is Δv (33). Equating the work done by surface

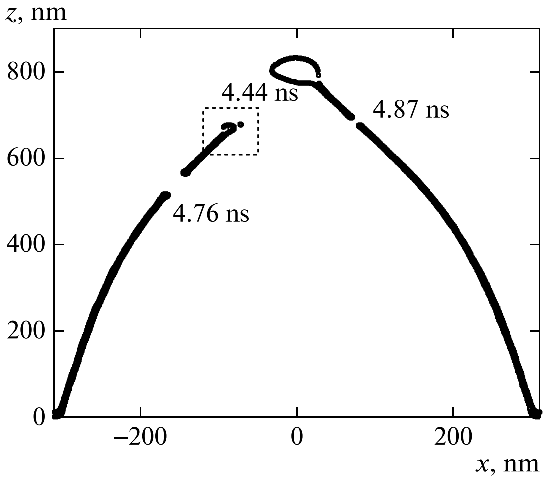

Fig. 34. Evolution of cupola for initial parameters specified in Fig. 30 (high initial velocity of 300 m/s); $t = 4.896$ ns. Clearly seen central drop and drops at banks of ruptures are indicated. Drop at right band of first rupture has merged with central drop. Instant of the given rupture is indicated. Drop at left bank of first rupture is shown in Fig. 35 on a large scale.

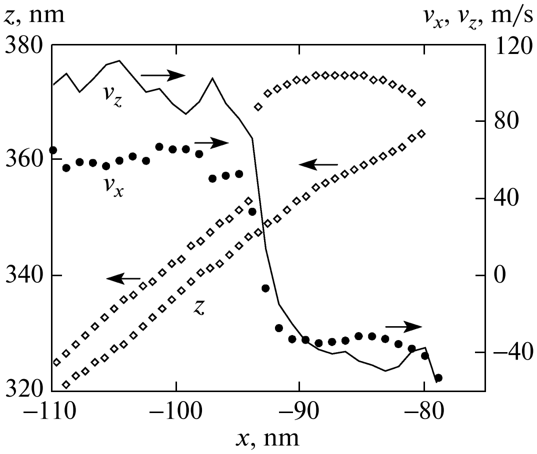

Fig. 35. Shape of region shown by rectangle in Fig. 34. Large drop and velocity jump associated with boundary between drop and film can be seen. This is shape of drop shown on left side of Fig. 33 at a later instant. Drop absorbs with time newer and newer portions of film and increases in size.

tension forces to the kinetic energy of the drop plus dissipated energy Q, we obtain

$$2l\sigma = kd_f\rho(\Delta v)^2/2 + Ql,$$

where the left-hand side is the spent capillary energy and the right-hand side is the sum of the kinetic energy of the drop and the energy converted into heat per unit area. Substituting velocity increment (33) into this relation, we find that half the surface energy is converted into the kinetic energy, and the other half dissipates ($Q = \sigma$). In the above formulas, we assumed that the film is thin. Therefore, the film surface area is much larger than the area of the drop formed from it. Therefore, we can disregard capillary energy of the drop.

The existence of relation (33) does not mean that on the film surface (i.e., outside the drop at the end of the film), wave equation (28) and expression (31) for the velocity of sound do not hold. Relation (33) implies that the end drop formed due to the rupture of the film moves at the velocity of sound (like the spall pulse). Therefore, a material particle of the film (right to its absorption by the drop) "does not know" that the rupture has occurred. Considering the Mach number, we note that during the ascent of the cupola to height $z \sim R_L$, the velocity of flow of the substance into the central drop is comparable to the velocity of sound (31), $\Delta v \approx 0.5 v_\sigma/\sqrt{2}$.

It should be emphasized that with increasing initial velocity v_o (18) and dimensionless key parameter $\hat{V}_o$ (13) (assuming that the values of σ and μ_o (16) are fixed), the direction (downward or upward) of the preferred emission of the mass of the gold film separated from the substrate changes. This can be seen from the curves in Figs. 24, 25, and 27. For $\hat{V}_o < A$, the main mass returns to the substrate, because in the opposite case the major part of the mass flies away (ablation); quantity $A \approx 1.8$. The concept "main mass" corresponds to the central drop that always moves approximately along the vertical (along the z axis). This is due to the approximate symmetry of the cupola. The angle of emission of a small droplet (if it exists) is determined by the vector of the momentum of the detached piece of the film prior to its separation from the main film. An example of such a piece is given in Fig. 34 (the piece between the ruptures at 4.76 and 4.44 ns). In the case represented in Fig. 29, the central drop hits the substrate. In the case illustrated in Fig. 30, the central drop moved upwards along the vertical.

3.7. Physical Reasons for the Flow of the Substance to the Axis and for the Jet Formation

Capillary forces basically change the form of motion of the film, in contrast to cases with zero surface tension (cf. curves *1–3* in Fig. 16 with curve *4*). The resistance of the surface of the cupola to its extension leads to the emergence of high acceleration and deceleration, $\partial^2 r/\partial t^2 \equiv a_r$ and $\partial^2 z/\partial t^2 \equiv a_z$. A typical example is shown in Fig. 36. The figure is the same as Fig. 16, in which accelerations leading to such displacements are shown instead of displacements. We did not indicate in Fig. 36 accelerations in the substance that entered into the loop (see Fig. 16). Dimensionless accelerations $\hat{a}$ in the capillary system of units

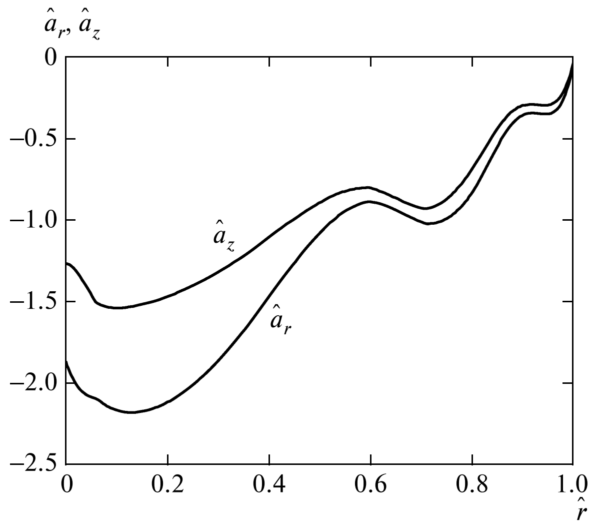

Fig. 36. Accelerations a_r of material particles of film towards z axis and deceleration a_z of particles along axis at instant $t = 1.846$ ns ($\hat{t} = 0.70954$). Parameters and instant correspond to axisymmetric (2D$_a$) laser action from Fig. 16.

are transformed into dimensional accelerations by the formula $|\partial^2 r/\partial t^2| = (v_\sigma^2/R_L)\hat{a}$. Substituting the parameters of the MD computation illustrated in Fig. 16 for acceleration scale v_σ^2/R_L, we obtain 4.4×10^{12} cm/s^2. This value is nine orders of magnitude higher than the acceleration due to gravity, two orders of magnitude higher than the free-fall acceleration on white dwarfs, and amounts to a few percent of the huge acceleration on neutron stars.

In the noninertial system of coordinates attached to decelerating cupola G (see Fig. 36), deceleration a_z is equivalent to that of the effective gravity field (bus deceleration effect), see Fig. 37. The acceleration component tangential to the cupola surface leads to the downward slip of the liquid towards the symmetry axis. This explains the origin of velocities directed to the center. The flow of the substance to the axis, first, causes a decrease in the film thickness in the cupola and, second, forms the bulk axial lump (see Fig. 22). The collision of the radial flow of the film with the axis leads to the emergence of a jet and a counterjet. This is a standard effect in the theory of collisions of jets [82, 83]. Thus, the physics of the nanostructuring in actual experiments [1, 2, 28–33, 86–88], in which nanojets and the counterjets were detected (see Fig. 7 in [28]), becomes clear. In previous theoretical constructions, the origin of the radial flow of the liquid phase to the central zone could not be explained.

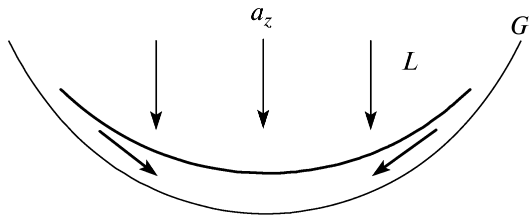

Fig. 37. Gravity field a_z in coordinate system attached to boundary G presses liquid L to boundary G. Sliding force is responsible for acceleration of liquid towards z axis. This picture explains emergence of central drop (see Figs. 16, 17, 22, 28–30, 33, 34) and axial jet (see Figs. 22 and 23).

4. CONCLUSIONS

The problem of the spatially localized action of laser radiation on a film target is important for many applications from microelectronics to biomedicine and nanoplasmonics [1, 2, 28–33, 86–88]. We have constructed a detailed model of the action on the film. The model includes the stage of spallation lasting tens of picoseconds, as well as the stage of evolution of the cupola lasting about 1–10 ns. The fine features of the interaction of hydrodynamic waves in the film and the substrate have been analyzed. The physical picture of separation (blistering) of the film from the substrate has been described. The ablation of thin films from a dielectric substrate has not been described earlier.

Although ideas about the thermomechanical nature of rapid (isochoric heating) ablation have been well developed at present [4, 5, 14–18, 44–47, 56, 63, 65, 67, 69, 89], we describe a number of new aspects. The relation between the absorbed fluence and the velocity of the gold film bounced from the substrate has been obtained (Section 2). A large-scale MD computation has been carried out in the axial geometry (Sections 3.2 and 3.3). It has been demonstrated how the nanojet is formed (see Fig. 22). The nonlinear system of partial differential equations describing the cupola flight has been analyzed (Sections 3.4 and 3.5). The effect of geometry (planar and axisymmetric cases, Section 3) has been considered. The case of low velocities of motion of the film from the substrate (linear theory, 2D$_a$ and 2D$_p$ cases; Sections 3.4 and 3.5, respectively) has been studied analytically. The decay of the film and formation of nanodrops have been analyzed (Section 3.6). A simple explanation has been obtained for the flow of the substance to the apical zone of the cupola (Section 3.7). It is this process that leads to the formation of jets and counterjets (Section 3.7).

ACKNOWLEDGMENTS

This study was supported by the Russian Science Foundation (project no. 14-19-01599). The molecular-dynamics simulation was carried out on the "Lomonosov" supercomputer of the Moscow State University.

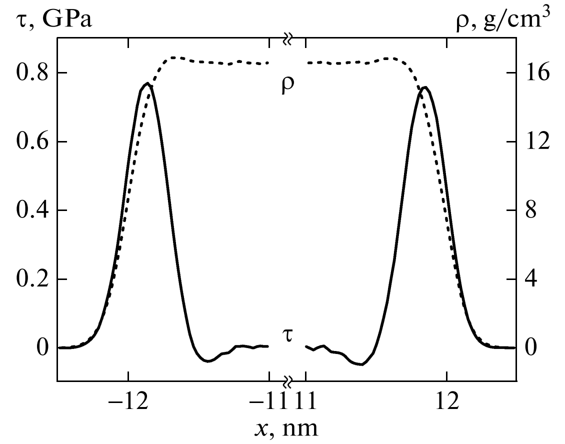

Fig. 38. Method for determining surface tension and thermodynamic parameters on binodal with the help of MD simulation; $\tau = (P_x - P_y)/2$.

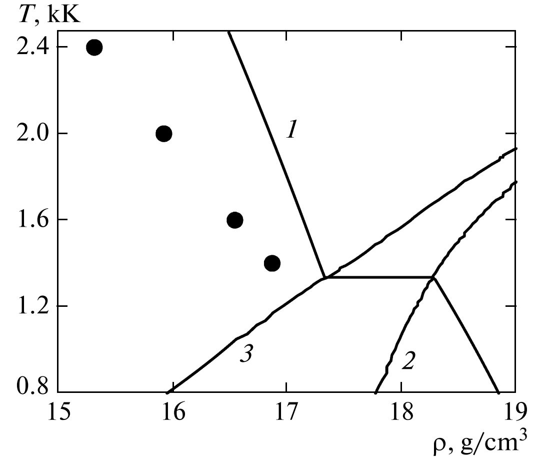

Fig. 39. Comparison of boiling curves (solid curves, EOS [36, 37, 53, 54]; markers correspond to the EAM potential): *1*—binodal; *2*—solidus; *3*—liquidus. Triple point corresponds to horizontal segment.

APPENDIX

Interparticle Potential, Binodal, and Surface Tension

In MD computations, we have used the interparticle potential of gold from [70]. This potential corresponds to the embedded atom method (EAM potential). Let us compare the results obtained using the equation of state [36, 37, 53, 54] and with the help of the EAM potential. The given equation of state was used in the hydrodynamic analysis of ablation of gold film from a substrate in Section 2. The method for determining the thermodynamic parameters is illustrated in Fig. 38. We take a gold film with a thickness of about 25 nm. The film has two free boundaries. Coordinate x in Fig. 38 is perpendicular to the plane of the film. The figure shows two near-boundary layers of the film on a large scale, and the middle part is omitted.

The method for determining the surface tension and thermodynamic parameters can be described as follows. The substance of the film is heated by a thermostat to a preset temperature. Then the system is kept thermostatic for a long time. The parameters are determined when the system attains thermal equilibrium. The values of surface tension for four temperatures determined in this way are given above in Fig. 15. It should be noted that these values satisfactorily fit into the $\sigma(T)$ curve from [75]. To determine σ, the net tangential pressure τ in Fig. 38 should be integrated with respect to coordinate x over both liquid-vapor interfaces.

Outside the film in Fig. 38, the pressure is low, and the film slowly evaporates (temperatures are also low). The boiling point of gold is 3243 K. At this temperature, the saturated vapor pressure above the gold melt attains one atmosphere. Even pressures of 100 atm are negligible, compared to shear stress τ in Fig. 38. Therefore, the presence of vapor does not affect the accuracy in determining the capillary factor in the temperature range under investigation.

The density of the substance in the central part of the film in Fig. 38 corresponds to the state on the binodal in accordance with the embedded atom method (EAM) potential used. The segment of the binodal we are interested in is referred to as the boiling curve. On this segment, the condensed phase (liquid) borders the vapor–liquid two-phase region. Comparison of the boiling curves obtained with the help of the equation of state and MD simulation is illustrated in Fig. 39. The MD values on the binodal are indicated by markers.

The EAM potential considerably reduces surface tension σ (by half; see Fig. 15). Conversely, thermal expansion coefficient $\beta = (\partial \ln V/\partial T)_p$ is overestimated (see Fig. 39). For this reason, the boiling curve obtained in the MD computations lies below. Accordingly, the critical temperature determined with the help of the EAM potential is lower, and the saturated vapor pressure is higher (at the same temperature). It is interesting that coefficients of thermal expansion β as well as σ differ by a factor of two: $\beta_{\text{EOS}} = 0.48 \times 10^{-4}$ K^{-1} and $\beta_{\text{EAM}} = 0.96 \times 10^{-4}$ K^{-1}. The error in determining $\beta \approx 0.43 \times 10^{-4}$ K^{-1} in the solid phase is much smaller. The parameters of the solid phase are described with the help of the EAM potential to a high degree of accuracy [70].

The EAM potential gives accurate values of the parameters of the triple point: melting temperature T_m and the difference in the densities of the solid and liquid phases. EAM potential [70] gives a value of 1330 K, while the reference value of T_m is 1337 K. Therefore, the MD boiling curve in Fig. 39 emerges from the left end of the segment corresponding to the triple point on the ρ, T plane. Quantity β is the differential coefficient; its computation involves differentiation. The density of the melt determined with the help of the EAM potential [70] is in good agreement with that obtained using the equation of state. Even at the point with the highest temperature (2.4 kK) in Fig. 39, the density is lower only by 8%.

REFERENCES

1. D. S. Ivanov, A. I. Kuznetsov, V. P. Lipp, B. Rethfeld, B. N. Chichkov, M. E. Garcia, and W. Schulz, Appl. Phys. A: Mater. Sci. Process. **111**, 675 (2013).
2. Y. P. Meshcheryakov, M. V. Shugaev, Th. Mattle, Th. Lippert, and N. M. Bulgakova, Appl. Phys. A: Mater. Sci. Process. **113**, 521 (2013).
3. K. Sokolowski-Tinten, J. Bialkowski, A. Cavalleri, D. von der Linde, A. Oparin, J. Meyer-ter-Vehn, and S. I. Anisimov, Phys. Rev. Lett. **81**, 224 (1998).
4. N. A. Inogamov, A. M. Oparin, Yu. V. Petrov, N. V. Shaposhnikov, S. I. Anisimov, D. von der Linde, and J. Meyer-ter-Vehn, JETP Lett. **69** (4), 310 (1999).
5. N. A. Inogamov, V. V. Zhakhovsky, Yu. V. Petrov, V. A. Khokhlov, S. I. Ashitkov, K. P. Migdal, D. K. Ilnitsky, Y. N. Emirov, K. V. Khishchenko, P. S. Komarov, V. V. Shepelev, M. B. Agranat, S. I. Anisimov, I. I. Oleynik, and V. E. Fortov, Proc. SPIE—Int. Soc. Opt. Eng. **9065**, 906502 (2013).
6. S. I. Anisimov, B. L. Kapeliovich, and T. L. Perel'man, Sov. Phys. JETP **39** (2), 375 (1974).
7. Yu. V. Petrov, N. A. Inogamov, and K. P. Migdal, JETP Lett. **97** (1), 20 (2013).
8. Z. Lin, L. V. Zhigilei, and V. Celli, Phys. Rev. B: Condens. Matter **77**, 075133 (2008).
9. K. P. Migdal, Yu. V. Petrov, and N. A. Inogamov, Proc. SPIE—Int. Soc. Opt. Eng. **9065**, 906503 (2013).
10. N. A. Inogamov, A. Ya. Faenov, V. V. Zhakhovsky, T. A. Pikuz, I. Yu. Skobelev, Yu. V. Petrov, V. A. Khokhlov, V. V. Shepelev, S. I. Anisimov, V. E. Fortov, Y. Fukuda, M. Kando, T. Kawachi, M. Nagasono, H. Ohashi, M. Yabashi, K. Tono, Y. Senda, T. Togashi, and T. Ishikawa, Contrib. Plasma Phys. **51**, 419 (2011).
11. Yu. V. Petrov and N. A. Inogamov, JETP Lett. **98** (5), 278 (2013).
12. N. A. Inogamov, S. I. Anisimov, and B. Retfel'd, J. Exp. Theor. Phys. **88** (6), 1143 (1999).
13. S. I. Anisimov, N. A. Inogamov, A. M. Oparin, B. Rethfeld, T. Yabe, M. Ogawa, and V. E. Fortov, Appl. Phys. A: Mater. Sci. Process. **69**, 617 (1999).
14. V. V. Zhakhovskii, K. Nishikhara, S. I. Anisimov, and N. A. Inogamov, JETP Lett. **71** (4), 167 (2000).
15. L. V. Zhigilei and B. J. Garrison, J. Appl. Phys. **88**, 1281 (2000).
16. S. I. Anisimov, V. V. Zhakhovskii, N. A. Inogamov, K. Nishihara, A. M. Oparin, and Yu. V. Petrov, JETP Lett. **77** (11), 606 (2003).
17. P. Lorazo, L. J. Lewis, and M. Meunier, Phys. Rev. Lett. **91**, 225502 (2003).
18. M. E. Povarnitsyn, T. E. Itina, M. Sentis, K. V. Khishchenko, and P. R. Levashov, Phys. Rev. B: Condens. Matter **75**, 235414 (2007).
19. F. Baset, K. Popov, A. Villafranca, J.-M. Guay, Z. Al-Rekabi, A. E. Pelling, L. Ramunno, and R. Bhardwaj, Opt. Express **21**, 12527 (2013).
20. B. Nagler, U. Zastrau, R. R. Fäustlin, S. M. Vinko, T. Whitcher, A. J. Nelson, R. Sobierajski, J. Krzywinski, J. Chalupsky, E. Abreu, S. Bajt, T. Bornath, T. Burian, H. Chapman, J. Cihelka, T. Döppner, S. Düsterer, T. Dzelzainis, M. Fajardo, E. Förster, C. Fortmann, E. Galtier, S. H. Glenzer, S. Göde, G. Gregori, V. Hajkova, P. Heimann, L. Juha, M. Jurek, F. Y. Khattak, A. R. Khorsand, D. Klinger, M. Kozlova, T. Laarmann, H. J. Lee, R. W. Lee, K.-H. Meiwes-Broer, P. Mercere, W. J. Murphy, A. Przystawik, R. Redmer, H. Reinholz, D. Riley, G. Röpke, F. Rosmej, K. Saksl, R. Schott, R. Thiele, J. Tiggesbäumker, S. Toleikis, T. Tschentscher, I. Uschmann, H. J. Vollmer, J. S. Wark, and B. Nagler, Nat. Phys. **5**, 693 (2009).
21. J. Colgan, J. Abdallah, Jr., A. Ya. Faenov, S. A. Pikuz, E. Wagenaars, N. Booth, O. Culfa, R. J. Dance, R. G. Evans, R. J. Gray, T. Kaempfer, K. L. Lancaster, P. McKenna, A. L. Rossall, I. Yu. Skobelev, K. S. Schulze, I. Uschmann, A. G. Zhidkov, and N. C. Woolsey, Phys. Rev. Lett. **110**, 125001 (2013).
22. B. L. Henke, E. M. Gullikson, and J. C. Davis, At. Data Nucl. Data Tables **54**, 181 (1993).
23. N. A. Inogamov, A. Ya. Faenov, V. V. Zhakhovskii, I. Yu. Skobelev, V. A. Khokhlov, Y. Kato, M. Tanaka, T. A. Pikuz, M. Kishimoto, M. Ishino, M. Nishikino, Y. Fukuda, S. V. Bulanov, T. Kawachi, Yu. V. Petrov, S. I. Anisimov, and V. E. Fortov, Contrib. Plasma Phys. **51**, 361 (2011).
24. M. Ishino, A. Ya. Faenov, M. Tanaka, S. Tamotsu, N. Hasegawa, M. Nishikino, T. A. Pikuz, T. Kaihori, and T. Kawachi, Appl. Phys. A: Mater. Sci. Process. **110**, 179 (2013).
25. M. Ishino, A. Ya. Faenov, M. Tanaka, S. Tamotsu, T. Pikuz, N. Hasegawa, M. Nishikino, N. Inogamov, I. Skobelev, V. Fortov, G. Norman, S. Starikov, V. Stegailov, T. Kaihori, T. Kawachi, and M. Yamagiwa, Proc. SPIE—Int. Soc. Opt. Eng. **8849**, 88490F (2013). doi 10.1117/12.2022425
26. E. N. Borodin, A. E. Mayer, and V. S. Krasnikov, Curr. Appl. Phys. **11**, 1315 (2011).
27. P. K. Patel, A. J. Mackinnon, M. H. Key, T. E. Cowan, M. E. Foord, M. Allen, D. F. Price, H. Ruhl, P. T. Springer, and R. Stephens, Phys. Rev. Lett. **91**, 125004 (2003).
28. C. Unger, J. Koch, L. Overmeyer, and B. N. Chichkov, Opt. Express **20**, 24864 (2012).
29. Y. Nakata, T. Okada, and M. Maeda, Jpn. J. Appl. Phys. **42**, L1452 (2003).
30. F. Korte, J. Koch, and B. N. Chichkov, Appl. Phys. A: Mater. Sci. Process. **79**, 879 (2004).
31. Y. Nakata, N. Miyanaga, and T. Okada, Appl. Surf. Sci. **253**, 6555 (2007).
32. A. I. Kuznetsov, J. Koch, and B. N. Chichkov, Appl. Phys. A: Mater. Sci. Process. **94**, 221 (2009).
33. V. I. Emel'yanov, D. A. Zayarniy, A. A. Ionin, I. V. Kiseleva, S. I. Kudryashov, S. V. Makarov, T. H. T. Nguyen, and A. A. Rudenko, JETP Lett. **99** (9), 518 (2014).

34. N. A. Inogamov, V. V. Zhakhovskii, S. I. Ashitkov, V. A. Khokhlov, Yu. V. Petrov, P. S. Komarov, M. B. Agranat, S. I. Anisimov, and K. Nishihara, Appl. Surf. Sci. 255, 9712 (2009); N. A. Inogamov, V. V. Zhakhovskii, S. I. Ashitkov, V. A. Khokhlov, Yu. V. Petrov, P. S. Komarov, M. B. Agranat, S. I. Anisimov, and K. Nishihara, Appl. Surf. Sci. **255**, 9712 (2009); arXiv:0812.2965.
35. N. A. Inogamov, Yu. V. Petrov, V. V. Zhakhovsky, V. A. Khokhlov, B. J. Demaske, S. I. Ashitkov, K. V. Khishchenko, K. P. Migdal, M. B. Agranat, S. I. Anisimov, V. E. Fortov, and I. I. Oleynik, AIP Conf. Proc. **1464**, 593 (2012).
36. A. V. Bushman, I. V. Lomonosov, and V. E. Fortov, *Equations of State of Metals at High Energy Densities* (Institute of Chemical Physics, Russian Academy of Sciences, Chernogolovka, Moscow oblast, 1992) [in Russian].
37. A. V. Bushman, G. I. Kanel', A. L. Ni, and V. E. Fortov, *Intense Dynamic Loading of Condensed Matter* (Taylor and Francis, New York, 1993).
38. D. M. Medvedev and, Yu. V. Petrov, J. Exp. Theor. Phys. **88** (1), 128 (1999).
39. V. Recoules, J. Clerouin, G. Zerah, P. M. Anglade, and S. Mazevet, Phys. Rev. Lett. **96**, 055503 (2006).
40. M. B. Agranat, N. E. Andreev, S. I. Ashitkov, M. E. Veisman, P. R. Levashov, A. V. Ovchinnikov, D. S. Sitnikov, V. E. Fortov, and K. V. Khishchenko, JETP Lett. **85** (6), 271 (2007).
41. M. E. Veysman, M. B. Agranat, N. E. Andreev, S. I. Ashitkov, V. E. Fortov, K. V. Khishchenko, O. F. Kostenko, P. R. Levashov, A. V. Ovchinnikov, and D. S. Sitnikov, J. Phys. B: At., Mol. Opt. Phys. **41**, 125704 (2008).
42. S. Khakshouri, D. Alfe, and D. M. Duffy, Phys. Rev. B: Condens. Matter **78**, 224304 (2008).
43. P. R. Levashov, G. V. Sin'ko, N. A. Smirnov, D. V. Minakov, O. P. Shemyakin, and K. V. Khishchenko, J. Phys.: Condens. Matter. **22**, 505501 (2010).
44. E. G. Gamaly, Phys. Rep. **508**, 91 (2011).
45. P. A. Loboda, N. A. Smirnov, A. A. Shadrin, and N. G. Karlykhanov, High Energy Density Phys. **7**, 361 (2011).
46. S. V. Starikov, V. V. Stegailov, G. E. Norman, V. E. Fortov, M. Ishino, M. Tanaka, N. Hasegawa, M. Nishikino, T. Ohba, T. Kaihori, E. Ochi, T. Imazono, T. Kavachi, S. Tamotsu, T. A. Pikuz, I. Yu. Skobelev, and A. Ya. Faenov, JETP Lett. **93** (11), 642 (2011).
47. S. G. Bezhanov, A. P. Kanavin, and S. A. Uryupin, Kvantovaya Elektron. (Moscow) **41**, 447 (2011).
48. G. E. Norman, S. V. Starikov, and V. V. Stegailov, J. Exp. Theor. Phys. **114** (5), 792 (2012).
49. G. Norman, S. Starikov, V. Stegailov, V. Fortov, I. Skobelev, T. Pikuz, A. Faenov, S. Tamotsu, Y. Kato, M. Ishino, M. Tanaka, N. Hasegawa, M. Nishikino, T. Ohba, T. Kaihori, Y. Ochi, T. Imazono, Y. Fukuda, M. Kando, and T. Kawachi, J. Appl. Phys. **112**, 013104 (2012).
50. G. V. Sin'ko, N. A. Smirnov, A. A. Ovechkin, P. R. Levashov, and K. V. Khishchenko, High Energy Density Phys. **9**, 309 (2013).
51. G. E. Norman, S. V. Starikov, V. V. Stegailov, I. M. Saitov, and P. A. Zhilyaev, Contrib. Plasma Phys. **53**, 129 (2013).
52. Ya. B. Zel'dovich and Yu. P. Raizer, *Physics of Shock Waves and High-Temperature Hydrodynamic Phenomena* (Nauka, Moscow, 1966; Dover, New York, 2002).
53. http://teos.ficp.ac.ru/rusbank/.
54. K. V. Khishchenko, Tech. Phys. Lett. **30** (10), 829 (2004).
55. N. A. Inogamov, V. V. Zhakhovsky, V. A. Khokhlov, S. I. Ashitkov, Y. N. Emirov, K. V. Khichshenko, A. Ya. Faenov, T. A. Pikuz, M. Ishino, M. Kando, N. Hasegawa, M. Nishikino, P. S. Komarov, B. J. Demaske, M. B. Agranat, S. I. Anisimov, T. Kawachi, and I. I. Oleynik, J. Phys.: Conf. Ser. **510**, 012041 (2014).
56. N. A. Inogamov, V. V. Zhakhovsky, V. A. Khokhlov, B. J. Demaske, K. V. Khishchenko, and I. I. Oleynik, J. Phys.: Conf. Ser. **500**, 192023 (2014).
57. V. V. Stegailov, Contrib. Plasma Phys. **50**, 31 (2010).
58. D. Fisher, M. Fraenkel, Z. Henis, E. Moshe, and S. Eliezer, Phys. Rev. E: Stat., Nonlinear, Soft Matter Phys. **65**, 016409 (2001).
59. *Handbook of Physical Quantities*, Ed. by I. S. Grigoriev and E. Z. Meilikhov (Energoatomizdat, Moscow, 1991; CRC Press, Boca Raton, Florida, United States, 1997).
60. W. Ebeling, A. Foerster, V. Fortov, V. K. Gryaznov, and A. Ya. Polishchuk, *Thermophysical Properties of Hot Dense Plasmas* (Teubner, Stuttgart, Germany, 1991).
61. A. Yu. Kuksin, G. E. Norman, V. V. Stegailov, and A. V. Yanilkin, Comput. Phys. Commun. **177**, 34 (2007).
62. D. K. Ilnitsky, V. A. Khokhlov, N. A. Inogamov, V. V. Zhakhovsky, Y. V. Petrov, K. V. Khishchenko, K. P. Migdal, and S. I. Anisimov, J. Phys.: Conf. Ser. **500**, 032021 (2014).
63. A. K. Upadhyay, N. A. Inogamov, B. Rethfeld, and H. M. Urbassek, Phys. Rev. B: Condens. Matter **78**, 045437 (2008).
64. Ya. Cherednikov, N. A. Inogamov, and H. M. Urbassek, J. Opt. Soc. Am. B **28**, 1817 (2011).
65. B. J. Demaske, V. V. Zhakhovsky, N. A. Inogamov, and I. I. Oleynik, Phys. Rev. B: Condens. Matter **82**, 064113 (2010).
66. B. Chimier and V. T. Tikhonchuk, Phys. Rev. B: Condens. Matter **79**, 184107 (2009).
67. L. V. Zhigilei, Zh. Lin, and D. S. Ivanov, J. Phys. Chem. C **113**, 11892 (2009).
68. M. E. Povarnitsyn, T. E. Itina, K. V. Khishchenko, and P. R. Levashov, Appl. Surf. Sci. **253**, 6343 (2007).
69. A. N. Volkov and L. V. Zhigilei, J. Phys.: Conf. Ser. **59**, 640 (2007).
70. V. V. Zhakhovskii, N. A. Inogamov, Yu. V. Petrov, S. I. Ashitkov, and K. Nishihara, Appl. Surf. Sci. **255**, 9592 (2009).
71. N. A. Inogamov, A. Ya. Faenov, V. A. Khokhlov, V. V. Zhakhovskii, Yu. V. Petrov, I. Yu. Skobelev, K. Nishihara, Y. Kato, M. Tanaka, T. A. Pikuz, M. Kishimoto, M. Ishino, M. Nishikino, Y. Fukuda, S. V. Bulanov, T. Kawachi, S. I. Anisimov, and V. E. Fortov, Contrib. Plasma Phys. **49**, 455 (2009).

72. N. A. Inogamov and V. V. Zhakhovskii, JETP Lett. **100** (1), 4 (2014).

73. F. Aqra and A. Ayyad, Mater. Lett. **65**, 2124 (2011).

74. E. B. Webb III and G. S. Grest, Phys. Rev. Lett. **86**, 2066 (2001).

75. V. K. Semenchenko, *Surface Phenomena in Metals and Alloys* (Pergamon, New York, 1961).

76. V. V. Zhakhovskii, N. A. Inogamov, and K. Nishihara, JETP Lett. **87** (8), 423 (2008).

77. V. Zhakhovskii, N. Inogamov, and K. Nishihara, J. Phys.: Conf. Ser. **112**, 042080 (2008).

78. S. I. Ashitkov, N. A. Inogamov, V. V. Zhakhovskii, Yu. N. Emirov, M. B. Agranat, I. I. Oleinik, S. I. Anisimov, and V. E. Fortov, JETP Lett. **95** (4), 176 (2012).

79. E. V. Golosov, A. A. Ionin, Yu. R. Kolobov, S. I. Kudryashov, A. E. Ligachev, Yu. N. Novoselov, L. V. Seleznev, and D. V. Sinitsyn, J. Exp. Theor. Phys. **113** (1), 14 (2011).

80. J. Reif, Springer Ser. Mater. Sci. **130**, 19 (2010).

81. A. Ya. Vorobyev and Chunlei Guo, Opt. Express **14**, 2164 (2006).

82. G. Birkhoff and E. H. Zarantonello, *Jets, Wakes, and Cavities* (Academic, New York, 1957).

83. M. A. Lavrent'ev and B. V. Shabat, *Problems of Hydrodynamics and Their Mathematical Models* (Nauka, Moscow, 1973) [in Russian].

84. N. A. Inogamov, V. V. Zhakhovsky, S. I. Ashitkov, Y. N. Emirov, A. Y. Faenov, T. A. Pikuz, M. Ishino, M. Kando, N. Hasegawa, M. Nishikino, T. Kawachi, M. B. Agranat, A. V. Andriash, S. E. Kuratov, and I. I. Oleynik, J. Phys.: Conf. Ser. **500**, 112070 (2014).

85. N. A. Inogamov, V. V. Zhakhovskii, S. I. Ashitkov, Yu. V. Petrov, M. B. Agranat, S. I. Anisimov, K. Nishihara, and V. E. Fortov, J. Exp. Theor. Phys. **107** (1), 1 (2008).

86. Y. P. Meshcheryakov and N. M. Bulgakova, Appl. Phys. A: Mater. Sci. Process. **82**, 363 (2006).

87. D. S. Ivanov, B. Rethfeld, G. M. O'Connor, T. J. Glynn, A. N. Volkov and L. V. Zhigilei, Appl. Phys. A: Mater. Sci. Process. **92**, 791 (2008).

88. D. S. Ivanov, Zh. Lin, B. Rethfeld, G. M. O'Connor, T. J. Glynn, and L. V. Zhigilei, J. Appl. Phys. **107**, 013519 (2010).

89. A. A. Ionin, S. I. Kudryashov, L. V. Seleznev, D. V. Sinitsyn, A. F. Bunkin, V. N. Lednev, and S. M. Pershin, J. Exp. Theor. Phys. **116** (3), 347 (2013).

Translated by N. Wadhwa